

Contents lists available at ScienceDirect

Journal of Computational Physics

www.elsevier.com/locate/jcp



Stable *a posteriori* LES of 2D turbulence using convolutional neural networks: Backscattering analysis and generalization to higher *Re* via transfer learning



Yifei Guan a,*, Ashesh Chattopadhyay a, Adam Subel a, Pedram Hassanzadeh a,b,*

- ^a Department of Mechanical Engineering, Rice University, Houston, TX, 77005. United States
- ^b Department of Earth, Environmental and Planetary Sciences, Rice University, Houston, TX, 77005, United States

ARTICLE INFO

Article history: Received 22 February 2021 Received in revised form 6 January 2022 Accepted 20 February 2022 Available online 25 February 2022

Keywords:
Large-eddy simulation
Subgrid-scale modeling
Deep Learning
Transfer learning
Convolutional neural networks
Data-driven modeling

ABSTRACT

There is a growing interest in developing data-driven subgrid-scale (SGS) models for largeeddy simulation (LES) using machine learning (ML). In a priori (offline) tests, some recent studies have found ML-based data-driven SGS models that are trained on high-fidelity data (e.g., from direct numerical simulation, DNS) to outperform baseline physics-based models and accurately capture the inter-scale transfers, both forward (diffusion) and backscatter. While promising, instabilities in a posteriori (online) tests and inabilities to generalize to a different flow (e.g., with a higher Reynolds number, Re) remain as major obstacles in broadening the applications of such data-driven SGS models. For example, many of the same aforementioned studies have found instabilities that required often ad-hoc remedies to stabilize the LES at the expense of reducing accuracy. Here, using 2D decaying turbulence as the testbed, we show that deep convolutional neural networks (CNNs) can accurately predict the SGS forcing terms and the inter-scale transfers in a priori tests, and if trained with enough samples, lead to stable and accurate a posteriori LES-CNN. Further analysis attributes aforementioned instabilities to the disproportionately lower accuracy of the CNNs in capturing backscattering (anti-diffusion) when the training set is small. We also show that transfer learning, which involves re-training the CNN with a small amount of data (e.g., 1%) from the new flow, enables accurate and stable a posteriori LES-CNN for flows with 16× higher Re (as well as higher grid resolution if needed). These results show the promise of CNNs with transfer learning to provide stable, accurate, and generalizable LES for practical use.

© 2022 Elsevier Inc. All rights reserved.

1. Introduction

Accurate simulations of turbulent flows are of critical importance for predicting and understanding various engineering and natural systems. However, the direct numerical simulation (DNS) of the Navier-Stokes equations remains computationally prohibitive for many real-world applications because DNS requires resolving (i.e., directly solving for) all the relevant spatial and temporal scales. These scales might span several orders of magnitude, e.g., from the domain length down to the Kolmogorov scale [77,97]. Large-eddy simulation (LES) offers a balance between accuracy and computational cost, since in LES, only the part of the inertial range containing the large-scale structures is resolved on a coarse-resolution grid and the

E-mail addresses: yifei.guan@rice.edu (Y. Guan), pedram@rice.edu (P. Hassanzadeh).

^{*} Corresponding authors.

effects of the subgrid-scale (SGS) eddies are parameterized, in terms of the resolved flow, using a SGS model [97,103]. As a result, the quality of the solutions from LES highly depends on the quality of the SGS model. Consequently, formulating accurate SGS models for LES has been an active area of research for the past few decades in different disciplines [e.g., 24,73,99,103,106,107]. Below, we briefly describe some of the key physics-based SGS models and their major shortcomings, which have motivated the recent interest in using machine learning (ML) to find data-driven SGS models. Then, we discuss some of the advances in data-driven SGS modeling as well as the main challenges, some of which we aim to address in this paper.

In his pioneering work on developing one of the first global climate models, Smagorinsky proposed a physics-based SGS model for LES in 1963 [111]. In this model (SMAG, hereafter), effects of the SGS eddies are parameterized as a function of the resolved flow using a scale-selective dissipative model that consists of a positive eddy viscosity ν_e and second-order diffusion. Since then, the SMAG model and its variants have been widely used in different disciplines, for example, to simulate weather and climate variability, combustion, multiphase flows, wind farms, and magnetohydrodynamics [e.g., 1,33,34,51,93,96,102,113,118]. Such purely diffusive SGS models lead to numerically stable LES; however, they might not correctly capture the inter-scale physical processes such as energy (and enstrophy) transfers. These models often include second-order dissipation but higher orders can also contribute to the forward transfer, i.e., transfer from the resolved scales to the subgrid scales [73]. Furthermore, while in the mean, the transfer is forward and the role of SGS processes is indeed dissipative, it is known that locally there can be transfer from the subgrid scales to the resolved scales. This process is referred to as backscattering, which is missing from purely diffusive SGS models [97].

Backscattering has been found to play a significant role in various fluid flows, and extensive work has been done in different disciplines to account for it in physics-based SGS models [e.g., 14,25,48,49,61,68,81,108,119,139]. For example, Piomelli et al. [94,95] showed that the lack of energy backscattering in LES could lead to inaccurate prediction of the perturbation growth in transitional wall-bounded flows. Backscattering has been also found to be important in geophysical turbulence, which has implications for modeling atmospheric and oceanic circulations and weather/climate predictions [9,39,42,44,79,101,109]. To improve the SMAG model and account for backscattering, Germano et al. [37] developed a dynamic approach to compute the eddy viscosity, which could lead to $\nu_e < 0$ (anti-diffusion) and account for backscattering. While this model (known as dynamic Smagorinsky; DSMAG hereafter) and its variants were shown to accurately represent many aspects of inter-scale energy transfers, it could also lead to numerical instabilities [63,74]. As a result, later modifications were proposed to enforce $\nu_e \ge 0$ as a tradeoff between numerical stability and backscattering [137]. Adding stochasticity to eddy-viscosity SGS models as well as other approaches have been proposed to improve their accuracy (e.g., account for backscattering) while maintaining stability [e.g., 14,16,25,26,43,44,66,67]. Despite these efforts, the need for better SGS models that accurately account for both forward and backscatter transfers remains. As a motivating example, the parameterizations currently used in global climate models do not account for kinetic energy backscattering [42].

In the past few years, there has been a rapidly growing interest in using ML methods to improve the modeling and analysis of chaotic systems and turbulent flows [e.g., 3,18,20,35,47,69,76,80,88,89,100,110,123,128]; also see the recent review papers on this topic [8,13,29,30,85]. Specific to SGS modeling (for LES or other approaches), a number of studies have aimed to obtain better estimates for the parameter(s) of physics-based SGS models, such as ν_e , from high-fidelity data (e.g., DNS or observations) [28,72,105,107,112,129]. Alternatively, a growing number of recent papers have aimed to learn a data-driven SGS model from high-fidelity data, often in a non-parametric fashion, i.e., without any prior assumption about the model's structural/functional form [e.g., 35,36,46,64,86,90,98,104,117,124,125]. In the studies from the latter category that focused on LES, a variety of canonical fluid systems and different approaches (e.g., local vs. non-local) have been investigated. In the local approach, which often employs multilayer perceptron artificial neural networks (ANNs), the SGS term (stress tensor or its divergence) at a grid point is estimated in terms of the resolved flow at or around the same grid point. For example, Maulik et al. [71] and Xie et al. [130,131] have, respectively, studied 2D decaying homogenous isotropic turbulence (2D-DHIT) and 3D incompressible and compressible turbulence using this approach (also, see [133]). In the non-local approach, which often employs variants of convolutional neural networks (CNNs), the SGS term over the entire domain is estimated in terms of the resolved flow in the entire domain to account for potential spatial correlations (e.g., due to coherent structures) and non-homogeneities in the system. For example, Zanna and Bolton [11,138], Beck and colleagues [7,55], Pawar et al. [91], and Subel et al. [115] have used this approach for ocean circulation, 3D-DHIT, 2D-DHIT, and forced 1D Burgers' turbulence,

In *a priori* (offline) tests, in which the accuracy of the SGS model in estimating the SGS term as a function of the resolved flow is evaluated, some of these studies have found the data-driven SGS models to accurately account for interscale transfers (including backscattering) and outperform physics-based models such as SMAG and DSMAG [11,71,91,138, 140]. However, most of the same studies have also found that in *a posteriori* (online) tests, in which the data-driven SGS model is coupled with a coarse-resolution numerical solver, the LES model is unstable, leading to numerical blow-up or physically unrealistic flows [7,8,55,71,114,132,138,140]. While the reason(s) for these instabilities remain unclear, a number of remedies have been proposed, e.g., post-processing of the trained SGS model to remove backscattering or to attenuate the SGS feedback into the numerical solver, or combining the data-driven model with an eddy viscosity model [7,71,138, 140] (also, see the excellent review by Beck and Kurz [8]). However, such remedies include ad-hoc components and often substantially take away the advantages gained from the non-parametric, data-driven approach.

Instabilities in *a posteriori* tests remain a major challenge to broadening the applications of ML-based data-driven SGS models for LES. Another major challenge is the generalization capability of the data-driven SGS models beyond the flow

from which the training data are obtained, e.g., extrapolation to turbulent flows with higher Reynolds numbers (*Re*). The ability to generalize is important for at least two reasons: i) High-fidelity data from usually expensive simulations (e.g., DNS) are needed to train data-driven SGS models and given the sharp increase in the computational cost of DNS with *Re*, the ability to effectively extrapolate to higher *Re* makes data-driven SGS models much more useful in practice; and ii) Some level of generalization capability in the data-driven SGS models is essential for the LES models to be robust and trustworthy. However, it is known that such extrapolations are challenging for neural networks in general [54]. In LES modeling, *a priori* tests in 3D-DHIT have shown that the performance of data-driven SGS models degrades when applied to *Re* higher than the one for which the model is trained. In *a posteriori* tests with multi-scale Lorenz 96 systems [21] and forced 1D Burgers' turbulence [115], we found inaccurate generalization to more chaotic systems or flows with higher *Re*, particularly in terms of short-term prediction and re-producing the long-term statistics of rare events. However, in both studies, we also found that transfer learning, which involves re-training (part of) the already trained neural network using a small amount of data from the new system [136], enables accurate generalization, e.g., to $10 \times$ higher *Re* [21,115]. While promising, the effectiveness of transfer learning in enabling generalization in more complex turbulent flows needs to be investigated.

Building on these earlier studies, here we use a deep CNN architecture to build a non-local data-driven SGS model for a 2D-DHIT system using DNS data, and aim to

- (a) Examine the accuracy of this SGS model in *a priori* (offline) tests, with regard to both predicting the SGS terms and capturing inter-scale transfers;
- (b) Evaluate the accuracy and stability of LES with this SGS model (LES-CNN) in *a posteriori* (online) tests, both in terms of short-term predictions and long-term statistics;
- (c) Assess the effectiveness of transfer learning in enabling accurate and stable generalization of LES-CNN to higher *Re* (up to 16×). We also show generalization to higher grid resolutions by adding an encoder-decoder architecture to the CNN.

For (a) and (b), we also present results from the SMAG, DSMAG, and a mixed model (discussed later in Section 3.4 and referred to as Mixed hereafter) as well as a local ANN-based data-driven SGS model.

The remainder of this paper is structured as follows. Governing equations of the 2D-DHIT system, the filtered equations, and the DNS and LES numerical solvers are presented in Section 2, followed by descriptions of the data-driven SGS models (training data and the CNN and ANN architectures) and the physics-based SGS models (SMAG, DSMAG, and Mixed) in Section 3. Results of the *a priori* and *a posteriori* tests as well as generalization to higher *Re* and/or resolutions via transfer learning are presented in Section 4. Conclusions and future work are discussed in Section 5.

2. DNS and LES: governing equations and numerical solvers

2.1. Governing equations

The dimensionless governing equations of 2D-DHIT in the vorticity (ω) and streamfunction (ψ) formulation in a doubly periodic x-y domain are

$$\frac{\partial \omega}{\partial t} + \mathcal{N}(\omega, \psi) = \frac{1}{Re} \nabla^2 \omega, \tag{1a}$$

$$\nabla^2 \psi = -\omega,\tag{1b}$$

where the nonlinear term $\mathcal{N}(\omega, \psi)$ represents advection

$$\mathcal{N}(\omega, \psi) = \frac{\partial \psi}{\partial y} \frac{\partial \omega}{\partial x} - \frac{\partial \psi}{\partial x} \frac{\partial \omega}{\partial y}.$$
 (2)

2D turbulence is a fitting prototype for many large-scale geophysical and environmental flows (where rotation and/or stratification dominate) and has been widely used as a testbed for novel techniques, including ML-based SGS modeling [e.g., 15,116,119–121]. In DNS, as discussed in detail in Section 2.2, Eqs. (1a)-(1b) are numerically solved at high spatio-temporal resolutions.

To find the equations for LES, we apply filtering (denoted by $\overline{(\cdot)}$ and defined later) to Eqs. (1a)-(1b) to obtain

$$\frac{\partial \overline{\omega}}{\partial t} + \mathcal{N}(\overline{\omega}, \overline{\psi}) = \frac{1}{Re} \nabla^2 \overline{\omega} + \underbrace{\mathcal{N}(\overline{\omega}, \overline{\psi}) - \overline{\mathcal{N}(\omega, \psi)}}_{\Pi}, \tag{3a}$$

$$\nabla^2 \overline{\psi} = -\overline{\omega}. \tag{3b}$$

Note that in deriving these equations, we assume that the filter commutes with the spatial (and temporal) derivative operators, which is the case for commonly used filters such as box, sharp spectral, and Gaussian filters [97,102] with linear kernels in Fourier space; the latter is used in this work (see Section 3.1). As discussed in Section 2.2, the numerical solution of Eqs. (3a)-(3b) requires spatio-temporal resolutions lower than those of the DNS. However, the SGS forcing term, Π ,

includes the effects of the small-scale eddies that have been truncated due to filtering/coarse-graining and are not resolved in LES. As a result, Π has to be estimated solely based on the resolved variables $(\overline{\omega}, \overline{\psi})$ to close Eqs. (3a)-(3b), which is the central task in turbulence modeling [97].

In most physics-based models, such as those using eddy viscosity, Π is modeled as a purely diffusive process (SMAG and DSMAG are described in Section 3.4). In data-driven approaches, such as the one pursued here and discussed in Sections 3.2 and 3.3, the aim is to learn the relationship between $(\overline{\omega}, \overline{\psi})$ and Π in DNS data using methods such as deep neural networks, without any prior assumptions about the functional form of this relationship.

2.2. Numerical solvers

For DNS, we solve Eqs. (1a)-(1b) in a doubly periodic square domain with $L \times L = [0, 2\pi] \times [0, 2\pi]$. A Fourier-Fourier pseudo-spectral solver is used along with second-order Adams-Bashforth and Crank-Nicolson time-integration schemes for the advection and viscous terms, respectively [2,5,41,45,50,125,140]. The computational grid has uniform spacing $\Delta_{\text{DNS}} = 2\pi/N_{\text{DNS}}$, where N_{DNS} is the number of grid points in each direction. We use $N_{\text{DNS}} = 2048$ for Re = 8000, 32000, and 64000, and $N_{\text{DNS}} = 3072$ for Re = 128000. For all DNS runs, $k_{\text{max}}l_{\text{V}} \ge 3.0$ and $k_{\text{max}}\eta \ge 1.5$, where k_{max} is the maximum wavenumber resolved on the computational grid, l_{V} is the enstrophy dissipation scale, and η is the Kolmogorov length scale, indicating that all DNS solutions are fully resolved [10,31,135,140]. The time-stepping size $\Delta t_{\text{DNS}} = 10^{-4}$ ($\Delta t_{\text{DNS}} = 5 \times 10^{-5}$) is used for $N_{\text{DNS}} = 2048$ ($N_{\text{DNS}} = 3072$). Following Refs. [70,71], the initial condition of each DNS run is a random vorticity field but with the same prescribed energy spectrum (see Appendix A for details). For each of the Re mentioned above, we conducted 15 independent DNS runs from random initial conditions.

The numerical solver is implemented in Python using CUDA GPU computing. We use equal numbers of GPU blocks as the resolution in each direction such that only one GPU thread in each block is assigned for the computation on one computational grid point. The fast Fourier transform (FFT) and inverse fast Fourier transform (iFFT) operations are performed using the cuFFT library. Double-precision floating-point arithmetic is used for all numerical solvers.

Fig. 1 shows an example of the vorticity field for Re=32000 at the initial condition (t=0), and at $t=50\tau$ and $t=200\tau$, where $\tau=1/|\omega|_{\text{max}}=0.02=200\Delta t_{\text{DNS}}$ ($|\omega|_{\text{max}}$ is computed at t=0). After around 50τ , the turbulent kinetic energy (TKE) spectrum $(\hat{E}(k))$ exhibits self-similarity. Note that the TKE spectrum is calculated using an angle average and therefore $k=\sqrt{k_x^2+k_y^2}$.

For LES, we solve Eqs. (3a)-(3b) using the same numerical solver used for DNS, except that the spatial resolution is lower by a factor of 8 in each direction (i.e., $N_{\text{LES}} = N_{\text{DNS}}/8$ and $\Delta_{\text{LES}} = 8\Delta_{\text{DNS}}$) and the time-stepping size is 10 times larger, $\Delta t_{\text{LES}} = 10\Delta t_{\text{DNS}}$. As a result, the LES solver requires 640 times fewer degrees of freedom, which substantially reduces the computational cost. However, the LES solver needs a SGS model for Π . Here, we use two data-driven models that employ CNN and ANN as well as three common physics-based models (SMAG, DSMAG, and Mixed). In the next section, we first describe the filtered DNS (FDNS) data, which are used for training the data-driven SGS models, and then describe the CNN, ANN, SMAG, DSMAG, and Mixed models.

3. Data-driven and physics-based SGS models for LES

3.1. Filtered DNS (FDNS) data

To compute the filtered DNS variables on the LES grid, which as mentioned above is $8 \times$ coarser than the DNS grid in each direction, we i) apply the Gaussian filter transfer function to the DNS data, and ii) coarse-grain the filtered results to the LES grid [97,138]. Below, the subscript "DNS" denotes the high-resolution DNS grid and "LES" denotes the coarse-resolution LES grid.

Using vorticity as an example, we first transform the DNS vorticity field $\omega(\mathbf{r}_{DNS})$ into the spectral space $\hat{\omega}(\mathbf{k}_{DNS})$, where $\mathbf{r} = (x, y)$ and $\mathbf{k} = (k_x, k_y)$. Then, we apply the Gaussian filter in the spectral space

$$\hat{\tilde{\omega}}(\mathbf{k}_{\text{DNS}}) = G(\mathbf{k}_{\text{DNS}}) \odot \hat{\omega}(\mathbf{k}_{\text{DNS}}). \tag{4}$$

where the operator \odot means element-wise multiplication of matrices and $(\tilde{\cdot})$ denotes the filtered variable at the DNS resolution. The transfer function of the Gaussian filter is [97]:

$$G(\mathbf{k}_{\text{DNS}}) = e^{-|\mathbf{k}_{\text{DNS}}|^2 \Delta_F^2 / 24},\tag{5}$$

where Δ_F is the filter size, which is taken to be $\Delta_F = 2\Delta_{LES}$ to yield sufficient resolution [97,140]. After the filtering operation, coarse-graining is performed to transform the filtered solution from the DNS to LES grid [97,138]:

¹ Neither the DNS nor LES solver is dealiased to avoid introducing any extra numerical dissipation. For selected cases, we have run dealiased DNS solvers and LES solvers (without any SGS model, LES-NM) using the Orszag Two-Third rule [12,83] and found quite similar TKE spectra produced by the dealiased and original solvers.

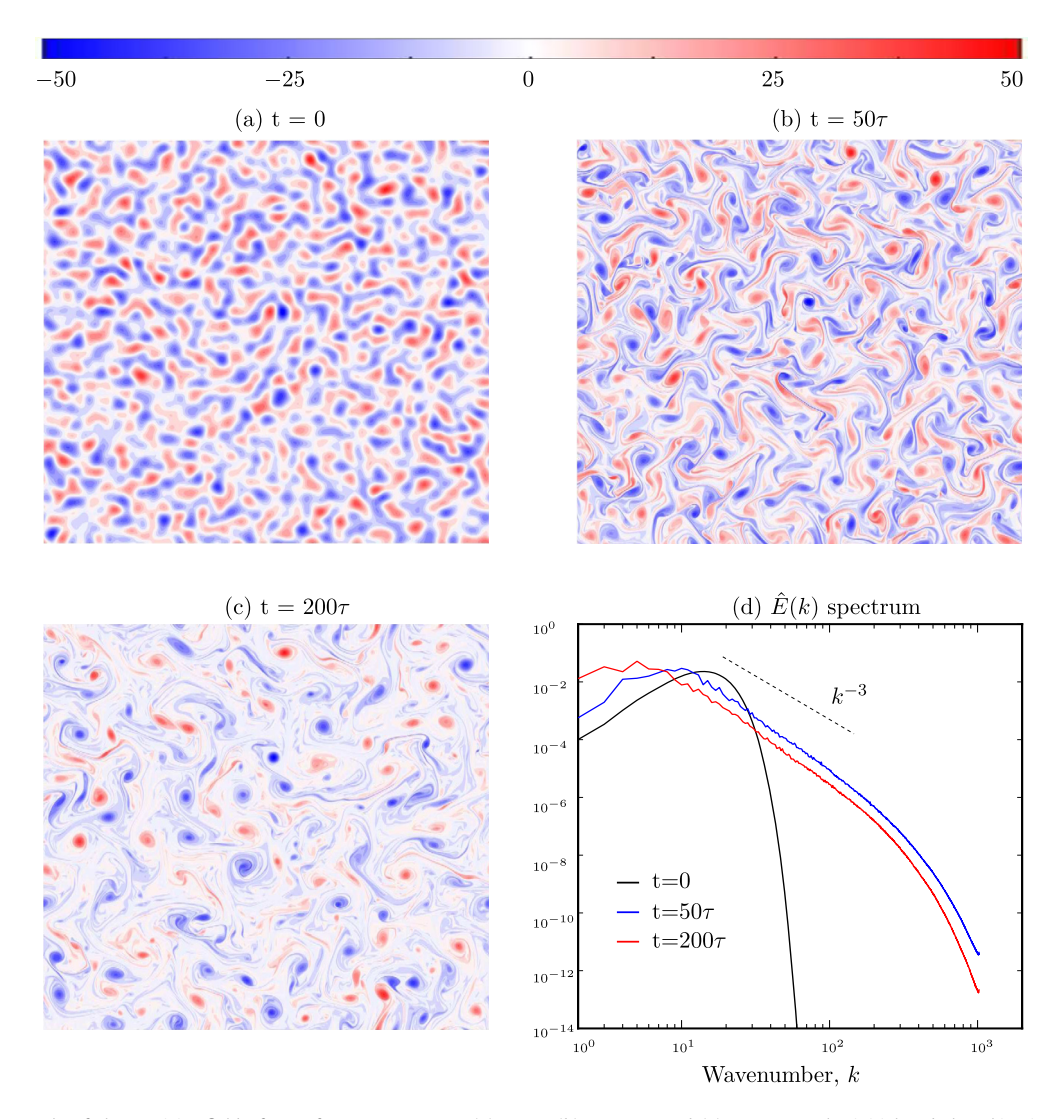


Fig. 1. An example of the vorticity field of DNS for Re = 32000 at (a) t = 0, (b) $t = 50\tau$, and (c) $t = 200\tau$. The initial turbulent kinetic energy (TKE) spectrum is prescribed while the vorticity field has random phase (see Appendix A). Data collection for training of data-driven SGS models (using CNN or ANN) starts from $t = 50\tau$ and ends at $t = 200\tau$. As shown in (d), in this period, the TKE spectra exhibit self-similarity following the k^{-3} scaling of the Kraichnan-Batchelor-Leith (KBL) theory [6,52,58]. (For interpretation of the colors in the figures, the reader is referred to the web version of this article.)

$$\overline{\hat{\omega}}(\mathbf{k}_{LES}) = \hat{\hat{\omega}}(|k_x| < k_c, |k_y| < k_c)$$
(6)

where $k_c = \pi/\Delta_{LES}$ is the cut-off wavenumber in spectral space, and we use $\overline{(\cdot)}$ to denote the filtered and then coarse-grained variables (hereafter, we use the term "filtered" for both "filtered" and then "coarse-grained" when there is no ambiguity). $\overline{\hat{\psi}}(\mathbf{k}_{LES})$ and $\hat{\Pi}(\mathbf{k}_{LES})$ are similarly computed following Eqs. (4)-(6).

Note that in addition to the Gaussian filter, box and sharp Fourier filters are also commonly used for LES. However, the Gaussian filter is compact in both physical and spectral spaces² [97]. Because our numerical solver is in the Fourier spectral space and our CNN and ANN operate in the physical space, we focus on the Gaussian filter for LES. Furthermore, Zhou et al. [140] found that the Gaussian filter outperforms the other two filters in terms of correlation coefficients of Π in their work on data-driven SGS modeling of 3D turbulence.

Fig. 2 shows examples of the Π term and effects of filtering on the vorticity field in physical space and on the TKE spectrum ($\hat{E}(k)$). The fine structures in DNS vorticity ω are lost in filtered vorticity $\tilde{\omega}$ and manifest themselves in SGS vorticity $\omega' = \omega - \tilde{\omega}$ and the SGS forcing term Π (panels (c)-(d)). The $\hat{E}(k)$ spectrum further shows the effects of the Gaussian filter on the energy at smaller scales (panel (e)). The Gaussian filter leads to the deviation of the FDNS spectrum from the DNS spectrum, especially at the scales near k_c .

² Compactness here means localized in the neighborhood of adjacent grid points and wavenumbers.

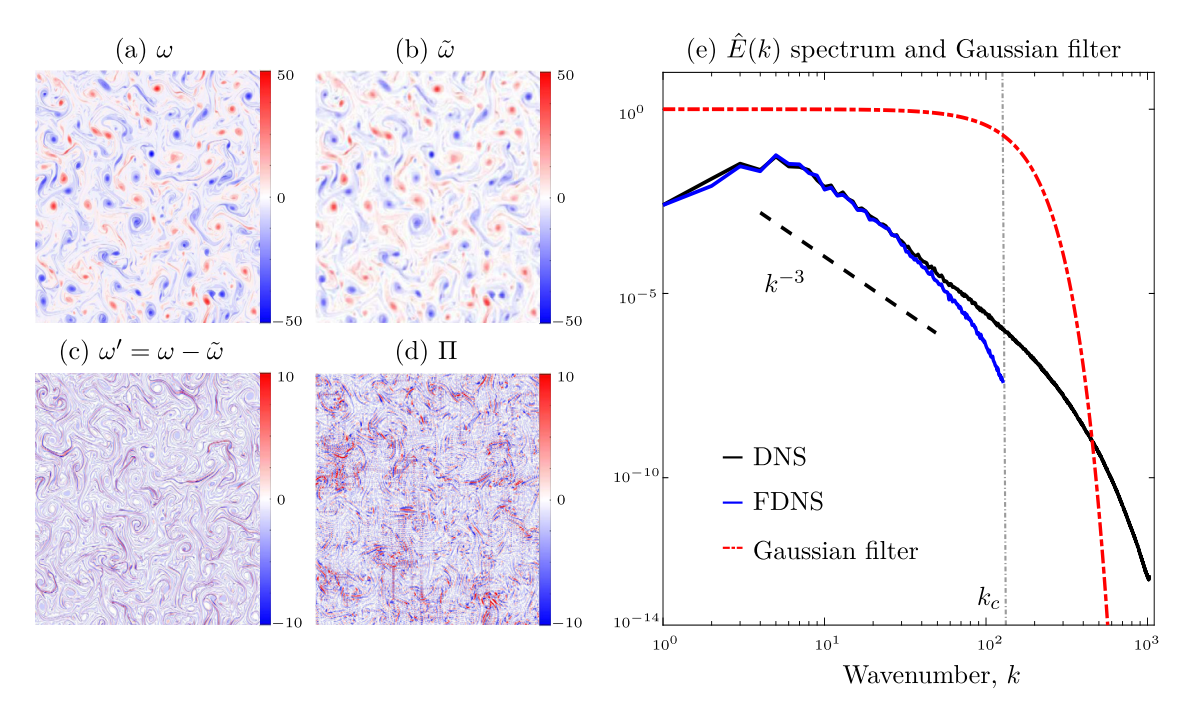


Fig. 2. Examples showing the effects of filtering. (a) DNS vorticity ω, (b) filtered vorticity $\tilde{ω}$, (c) SGS vorticity $ω' = ω - \tilde{ω}$, (d) SGS forcing term Π , and (e) TKE spectrum for Re = 32000 at the end of one of the DNS runs ($t = 200\tau$). Panel (e) also shows the transfer function of the Gaussian filter and the cutoff wavenumber, k_c . The FDNS spectrum deviates from the DNS spectrum near k_c because of the filtering.

Our goal is to non-parametrically learn Π as function of the FDNS variables $\overline{\omega}$ and $\overline{\psi}$ using a deep CNN as well as an ANN used in a previous study [71].

3.2. Convolutional neural network (CNN)

For non-local data-driven SGS modeling, we propose to use a deep CNN. The CNN architecture was originally developed for computer vision and image processing and its key feature is that rather than having pre-defined filters, CNNs learn the filters used for pattern recognition for a given data set [38,53,57]. CNNs have often been found superior to ANNs when the data contains spatial patterns and structures significant to the functional relationship to be learned [27,92]. Therefore, it is not surprising that CNNs have been found to perform well, usually superior to non-convolutional ML methods, in applications involving turbulent flows, given the abundance of coherent structures and spatial correlations in turbulence [e.g., 7,11,17,20,75,91]. Specifically for SGS modeling, a recent *a priori* analysis has shown that CNN outperforms local ANN in terms of prediction accuracy of the SGS stress term in the same 2D-DHIT system studied here [91].

Building on previous work and to account for non-local effects (e.g., coherent structures and spatial correlations), we use a CNN with inputs/outputs that are global (i.e., from the entire domain³). Thus, the input features are

$$\left\{ \frac{\overline{\psi}}{\sigma_{\overline{\psi}}}, \frac{\overline{\omega}}{\sigma_{\overline{\omega}}} \right\} \in \mathbb{R}^{2 \times N_{\text{LES}} \times N_{\text{LES}}}, \tag{7}$$

and the output targets are

$$\left\{\frac{\Pi}{\sigma_{\Pi}}\right\} \in \mathbb{R}^{N_{\text{LES}} \times N_{\text{LES}}},\tag{8}$$

where σ is the standard deviation of the corresponding variables calculated over all training samples. We aim to use a CNN to learn \mathbb{M} , an optimal map between the inputs and outputs

$$\mathbb{M}: \left\{ \overline{\psi} / \sigma_{\overline{\psi}}, \overline{\omega} / \sigma_{\overline{\omega}} \right\} \in \mathbb{R}^{2 \times N_{\text{LES}} \times N_{\text{LES}}} \to \left\{ \Pi / \sigma_{\Pi} \right\} \in \mathbb{R}^{\times N_{\text{LES}} \times N_{\text{LES}}} \tag{9}$$

³ Although in this work we use global inputs for CNN, in practical, realistic problems, where filtering the entire domain might be complicated or using large inputs might be prohibitive due to memory constraints, CNN can be applied to certain selected regions, as for example done in Ref. [40] for ocean modeling. The selection of these regions could be guided by the physical understanding of the system and other criteria such as spatial correlations.

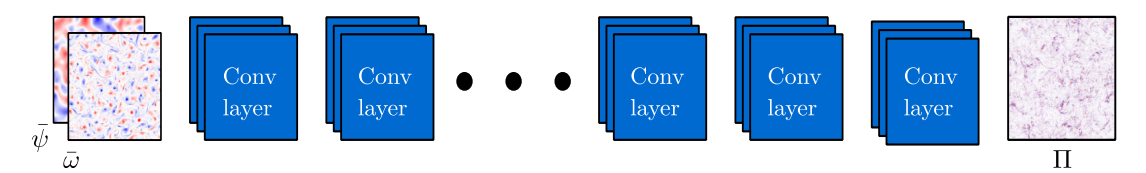


Fig. 3. Schematic of the CNN. Inputs and outputs are samples of normalized $(\bar{\psi}, \bar{\omega})$ and Π , respectively. The convolutional layers (Conv layers) have the same dimension (256 × 256) as that of the input and output layers. All Conv layers are initialized randomly and are trainable. The convolutional depth is set to 64, and the convolutional filter size is 5 × 5. The activation function of each layer is ReLu (rectified linear unit) except for the last one, which is a linear map.

by minimizing the mean-squared-error (MSE)

$$MSE = \frac{1}{n_{tr}} \sum_{i=1}^{n_{tr}} \| \Pi_i^{\text{CNN}} - \Pi_i^{\text{FDNS}} \|_2^2, \tag{10}$$

where n_{tr} is the number of training samples and $\|\cdot\|_2$ is the L_2 norm.

Fig. 3 schematically shows the CNN architecture that is used here. We use the mini-batch stochastic gradient descent method with the Adam optimizer to minimize the loss function, Eq. (10). Note that the CNN has no pooling or upsampling layers (i.e., *fully* CNN), so the hidden layers have the same size as the input and output layers. We have found that using a fully CNN is a key to training an accurate SGS model, consistent with earlier findings that pooling layers may artificially change spatial correlations of the data [20].⁴

Hyper-parameters such as the number of hidden layers have been determined via an extensive search. We find that to capture the complex pattern of Π , a deep CNN with 10 hidden layers is needed. For example, the 10-layer CNN outperforms shallower 8-layer and 5-layer CNNs in terms of training loss for the same n_{tr} . Moreover, we find that any networks with more than 10 layers would overfit the data and would lead to poorer performance as compared to the ones presented here. Overall, the CNN with 10 layers has 927041 trainable parameters.

The training, validation, and testing sets are generated using 2D snapshots of filtered data collected from 15 independent DNS runs with random initial conditions, sampled every $10\Delta_{DNS}$, in the time interval $[50\tau, 200\tau]$. We use the data from 8 runs for the training set, 2 runs for the validation set, and 5 runs for the testing set. The effects of the size of the training dataset on the accuracy of the SGS model are further discussed in Section 4.1.

As is the common practice in ML applications, we run the CNN (and the ANN) with single-precision floating-point operations during both training and testing to accelerate the process and reduce the data transfer/storage. We have also explored training/testing a CNN with double-precision floating-point arithmetic, but found no distinguishable enhancement in the *a posteriori* tests.

Finally, we point out that the codes for CNN and CNN with transfer learning (discussed later) are made publicly available on GitHub (see the Acknowledgments for details).

3.3. Multilayer perceptron artificial neural network (ANN)

A few recent studies have proposed building local data-driven SGS models using ANNs trained to learn the mapping between a local stencil of input variables to the local SGS term Π [71,131,133,140]. For example, Maulik et al. [71] employed such an approach for the same 2D-DHIT system and proposed to train an ANN with inputs consisting of 9 grid stencil values of $\overline{\omega}$ and $\overline{\psi}$ plus the local values of $|\overline{S}|$ and $|\nabla \overline{\omega}|$ and the output consisting of the local SGS term Π value:

$$\mathbb{M}: \left\{ \overline{\omega}_{i,j}, \overline{\omega}_{i,j+1}, ..., \overline{\omega}_{i-1,j-1}, \overline{\psi}_{i,j}, \overline{\psi}_{i,j+1}, ..., \overline{\psi}_{i-1,j-1}, |\overline{S}|_{i,j}, |\nabla \overline{\omega}|_{i,j} \right\} \in \mathbb{R}^{20} \to \left\{ \Pi_{i,j} \right\} \in \mathbb{R}^1, \tag{11}$$

where (i, j) here denotes a local grid point. $|\overline{S}|$ is the characteristic filtered rate of strain [97] and $|\nabla \overline{\omega}| = \sqrt{\left(\frac{\partial \overline{\omega}}{\partial x}\right)^2 + \left(\frac{\partial \overline{\omega}}{\partial y}\right)^2}$.

We have closely followed Ref. [71] in building a local data-driven SGS model. For the ANN, we use their publicly available code. The ANN is fully connected with 2 hidden layers, each containing 50 neurons. The network has 3651 trainable parameters. We explore architectures with more layers and neurons per layer, but find no improvement in the accuracy. Due to the use of local inputs (1 central grid point + 8 neighboring grid points), in this approach the number of training samples is equal to the number of snapshots multiplied by $N_{\rm LES}^2$. In common practice, only a few (less than 10) snapshots of data are used as the training data set [71,131,132,140]. Here, following Ref. [71], we use 8 randomly selected snapshots (from the training set mentioned in Section 3.2) resulting in 524288 samples in the training sets. We have also investigated

⁴ Fully CNN is used in all the cases of this work with an exception for the grid-extrapolation transfer learning (see Fig. 11) where one up/down sampling layer is used.

the effects of increasing the number of samples to 20 snapshots, but again, no substantial improvement in training loss is found. Note that following Ref. [71], no pre-processing, e.g., normalization, is performed on the input or output data.⁵

Note that it is not the purpose of this paper to compare the ANN- and CNN-based approaches side by side (even if such comparison is possible given the differences in architecture, network size, input/output, and size of the training set). Therefore, beyond the explorations mentioned above, we have not performed an exhaustive search on the ANN and local SGS modeling approach. Our explorations all suggest that the comprehensively investigated network/approach presented in Ref. [71] is already optimal.

3.4. Smagorinsky (SMAG), dynamics Smagorinsky (DSMAG), and Mixed SGS models

In the SMAG [111] model, which is a commonly used baseline SGS model for LES, the SGS stress term in the momentum equation is modeled as [97,102]:

$$\tau^{\text{SMAG}} = -2(C_s \Delta)^2 \langle 2\overline{S} \, \overline{S} \rangle^{1/2} \overline{S},\tag{12}$$

where the angle brackets $\langle \cdot \rangle$ denote domain averaging. \overline{S} is the filtered rate-of-strain tensor [97]. The SGS term Π in Eq. (3a) is therefore:

$$\Pi^{\text{SMAG}} = (C_s \Delta)^2 \langle 2\overline{S} \, \overline{S} \rangle^{1/2} \nabla^2 \overline{\omega} = \nu_e \nabla^2 \overline{\omega},\tag{13}$$

where C_s is the Smagorinsky coefficient, v_e is the eddy viscosity, and

$$\langle 2\overline{S}\,\overline{S}\rangle^{1/2} = \sqrt{4\left(\frac{\partial^2\overline{\psi}}{\partial x\partial y}\right)^2 + \left(\frac{\partial^2\overline{\psi}}{\partial x^2} - \frac{\partial^2\overline{\psi}}{\partial y^2}\right)^2}.$$
 (14)

 C_S is a constant in the SMAG model. The DSMAG model [37] uses a dynamic procedure to estimate ν_e based on the local flow structure. This procedure can lead to $\nu_e < 0$, which can result in numerical instabilities; consequently, "positive clipping" is often applied to enforce $\nu_e \ge 0$ [137]. Here, we use $C_S = 1$ for SMAG following Maulik et al. [71] and implement DSMAG (with positive clipping) following Pawar et al. [91], who studied the same 2D-DHIT system. Note that these SMAG and DSMAG models both have $\nu_e \ge 0$ and are therefore purely diffusive.

To also include a physics-based SGS model that captures backscattering among the baselines in some cases, here we use a mixed model [4,97,122,137] (Mixed), which combines the gradient model [23,59,60] and DSMAG with positive clipping. Mixed is implemented following Ref. [122]. Finally, in some cases, we also include results from LES with no SGS model, i.e., $\Pi = 0$ (LES-NM).

4. Results

4.1. A priori analysis

4.1.1. Accuracy

We first examine the accuracy of the CNN-based SGS model in predicting the Π term and inter-scale transfers for never-seen-before samples of $(\overline{\psi}, \overline{\omega})$ from the testing set. The results in Section 4.1.1 are reported for $n_{tr} = 50000$. We use a commonly used metric, the correlation coefficient c between the modeled (Π^M) and true (Π^{FDNS}) SGS terms defined as [7.91.139]:

$$c = \frac{\left\langle \left(\Pi^{M} - \langle \Pi^{M} \rangle \right) \left(\Pi^{\text{FDNS}} - \langle \Pi^{\text{FDNS}} \rangle \right) \right\rangle}{\sqrt{\left\langle (\Pi^{M} - \langle \Pi^{M} \rangle)^{2} \right\rangle} \sqrt{\left\langle (\Pi^{\text{FDNS}} - \langle \Pi^{\text{FDNS}} \rangle)^{2} \right\rangle}}.$$
(15)

The correlation coefficients (averaged over 100 random testing samples) for CNN as well as DSMAG, Mixed, and ANN are reported in Table 1. Consistent with the previous findings [36,91], *a priori* tests show that the data-driven SGS models substantially outperform DSMAG and Mixed, and that this CNN-based model (with *c* above 0.9) has statistically significantly higher accuracy than this ANN-based model. Note that similarly, previous findings based on correlation coefficients of SGS stress term found CNNs to outperform ANNs in *a priori* tests [91].

Next, we examine the inter-scale transfer in *a priori* tests. The transfer is often quantified using the SGS stress [97]. Since here we are working with the SGS forcing term Π , which is the curl of the divergence of the SGS stress, we instead follow previous work and define SGS transfer T as [48,71,119]:

⁵ We find both normalized and non-normalized data would lead to an unstable *a posteriori* analysis; however, in *a priori* analysis, normalizing the inputs and outputs leads to a \sim 5% increase in correlation coefficient *c*.

Table 1 Correlation coefficients c (Eq. (15)) between the predicted and true SGS term Π for Re=32000 in a priori tests. The subscripts indicate

SGS term Π for Re=32000 in a priori tests. The subscripts indicate c computed only over elements of Π^{FDNS} and Π^{M} corresponding to T>0 or T<0 (Eq. (16)). The values show the average over (the same) 100 randomly chosen testing samples and the standard deviation.

	DSMAG	Mixed	ANN	CNN
С	0.55 ± 0.06	0.68 ± 0.02	$\boldsymbol{0.86 \pm 0.02}$	0.93 ± 0.03
$c_{T>0}$	$\boldsymbol{0.55 \pm 0.06}$	$\boldsymbol{0.70 \pm 0.02}$	$\boldsymbol{0.86 \pm 0.02}$	$\boldsymbol{0.96 \pm 0.03}$
$c_{T<0}$	0	$\boldsymbol{0.50 \pm 0.04}$	$\boldsymbol{0.83 \pm 0.02}$	$\boldsymbol{0.92 \pm 0.04}$

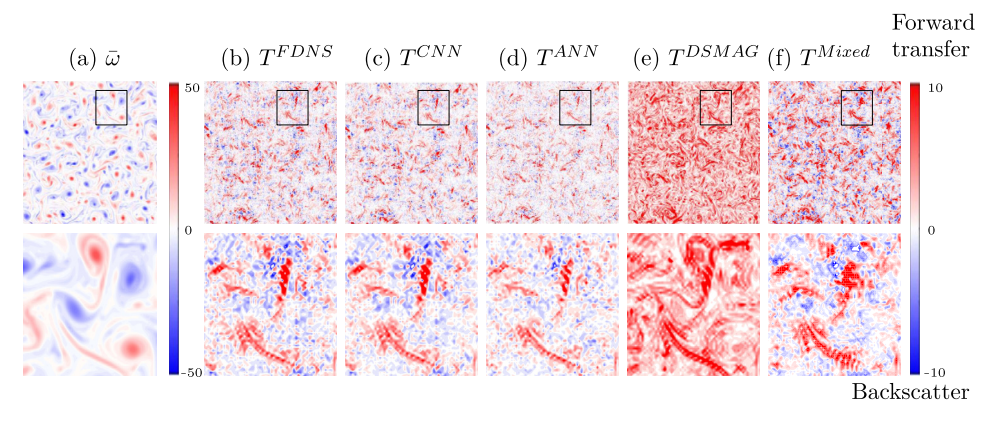


Fig. 4. Example of inter-scale transfer T, Eq. (16), in a priori analysis at Re = 32000. (a) Filtered vorticity $\overline{\omega}$; (b) true T from FDNS; (c)-(f) T from CNN, ANN, DSMAG, and Mixed. The ANN and CNN capture both forward transfer and backscatter while DSMAG only captures the forward transfer (diffusion). The Mixed can also capture both forward transfer and backscatter but the forward transfer is overestimated (more red), and therefore, in a posteriori analysis, LES-Mixed produces results that are more similar to LES-DSMAG (see Fig. 7). The upper row shows the entire domain while the second row shows the portion in the black square.

$$T = \operatorname{sgn}(\nabla^2 \overline{\omega}) \odot \Pi, \tag{16}$$

where $sgn(\cdot)$ is the sign function. At each grid point (i, j), $T_{i, j} > 0$ indicates forward transfer (diffusion of kinetic energy) while $T_{i, j} < 0$ indicates backscatter (anti-diffusion). Note that forward/backscatter is between the resolved and subgrid scales as separated by filtering, and should not be confused with the forward/inverse cascade, which is a physical property [97,120]. For a sample filtered vorticity $\overline{\omega}$, Fig. 4 shows the true inter-scale transfer T^{FDNS} and T from CNN, ANN, DSMAG, and Mixed. Because DSMAG is purely diffusive, it only captures the forward transfer. The ANN and CNN both capture the diffusion as well as backscattering. Table 1 further shows c computed separately over grid points corresponding to only T > 0 (diffusion) or only T < 0 (backscattering), again, demonstrating that the CNN-based SGS model captures both forward transfer of backscatter accurately, with c > 0.9.

To summarize, the *a priori* tests show that the CNN-based data-driven SGS model can accurately predict the out-of-sample SGS forcing terms and inter-scale transfers. However, as discussed in the Introduction, previous studies have found that accuracy in *a priori* tests does not necessarily translate to accuracy/stability in *a posteriori* analysis [7,71,138,140]. Before discussing the *a posteriori* tests in Section 4.2, we further examine how the accuracy of the CNN depends on the size of the training set, which as it turns out, impacts the stability of LES-CNN.

4.1.2. Scaling of the CNN's accuracy with size of the training set n_{tr}

Table 2 shows how the SGS term's correlation coefficient c varies in a priori tests as the number of samples used to train the CNN (n_{tr}) is increased. The value of c increases with n_{tr} , reaching 0.90 with $n_{tr} = 10000$ and 0.93 with $n_{tr} = 50000$. While c = 0.90 (for $n_{tr} = 10000$) might seem high enough and the CNN-based data-driven SGS model might seem accurate enough, a set of a posteriori tests with this LES-CNN model are found to lead to noisy, unphysical flows for some initial conditions. In fact, a posteriori tests with LES-CNN trained with lower n_{tr} (500 or 1000) lead to numerically unstable simulations that blow-up. Only simulations with $n_{tr} \geq 30000$ are found to lead to stable and accurate a posteriori LES-CNN for any initial condition.

The above analysis suggests that instabilities in *a posteriori* tests might be due to inaccurate out-of-sample predictions as a result of insufficient training data. These findings are consistent with our recent work on data-driven SGS modeling of forced 1D Burgers' turbulence with a non-local ANN [115], where we found unstable *a posteriori* LES-ANN, which was traced to inaccurate Π terms around some of the shockwaves. In that study, we showed that artificially enriching the training dataset using a data augmentation strategy [32,84,134] led to a stable and accurate LES-ANN.

Table 2 further reports $c_{T>0}$ and $c_{T<0}$ as a function of n_{tr} . This analysis shows that consistently, $c_{T<0}$ is lower than $c_{T>0}$, especially at small n_{tr} , but the difference declines from 0.15 to 0.04 with increasing n_{tr} . The implication of these results

Table 2

Correlation coefficients c (Eq. (15)) between the CNN-predicted and true SGS term Π for Re=32000 in a priori tests as a function of the number of training samples n_{tr} . The values show the average over (the same) 100 randomly chosen testing samples and the standard deviation. The last row indicates the fate of a posteriori LESCNN integrations from 5 random initial conditions: stable refers to numerically stable and accurate simulations, unstable refers to numerical blow-up, and unphysical refers to simulations leading to noisy/unrealistic flows (with substantial high-wavenumber structures and spuriously large vorticity values, see Appendix B for more details).

n _{tr}	500	1000	10000	30000	50000
с	0.78 ± 0.05	0.83 ± 0.04	0.90 ± 0.04	0.92 ± 0.04	0.93 ± 0.03
$c_{T>0}$	0.78 ± 0.05	0.86 ± 0.03	0.93 ± 0.04	0.95 ± 0.04	0.96 ± 0.03
$c_{T<0}$	0.63 ± 0.04	0.76 ± 0.03	0.89 ± 0.04	0.91 ± 0.04	0.92 ± 0.04
	unstable	unstable	unphysical	stable	stable

is that the SGS model with a CNN trained using a small n_{tr} is less capable of accurately predicting backscattering than forward transfer, which, based on previous findings, could lead to instabilities. As discussed in the Introduction, capturing backscattering is highly desired; however, it is known from physics-based SGS modeling efforts that it can lead to instabilities if handled incorrectly [63,74]. Moreover, in recent data-driven SGS modeling efforts, as discussed later, removing backscattering has been used as a way of stabilizing *a posteriori* LES [71,140]. Table 2 shows that at least for our CNN, the backscattering can be accurately captured and the *a posteriori* LES can be stable without any further post-processing if the training set is large enough.

In short, these results suggest that neural networks that may "seem" well-trained and accurate in *a priori* (offline) tests, may not be sufficient for stable/accurate LES in *a posteriori* (online) tests. We say "seem" because there is no established *a priori* metric and threshold to know if a data-driven SGS model is well-trained and accurate enough to lead to stable and accurate *a posteriori* LES. In this study, the threshold is empirically between c = 0.90 and c = 0.92, or if $c_{T<0}$ is a better metric, between 0.89 and 0.91. To be clear, these are just empirical thresholds in this testcase, and such thresholds might be case-dependent. Whether a general connection between a data-driven SGS models' accuracy in *a priori* tests and the *a posteriori* LES stability could be established or not should be thoroughly investigated in future work. Furthermore, we emphasize that we do not claim that all instabilities in other *a posteriori* LES runs using data-driven SGS models (reported in other studies) are due to similar inaccuracies that could be reduced by enriching the training set.

4.2. A posteriori analysis

In the *a posteriori* (online) tests, the CNN-based data-driven SGS model and the LES numerical solver of Eqs. (3a)-(3b) are coupled (LES-CNN): at a given time step, the resolved variables $(\overline{\psi}, \overline{\omega})$ from the numerical solver are normalized (dividing by their σ) and fed into the already trained CNN, which predicts Π^{CNN} . This Π^{CNN} is then de-normalized (multiplying by σ_{Π}) and fed back into the numerical solver to compute the resolved flow in the next time step, and the cycle continues. The CNN used for the *a posteriori* tests is trained with $n_{tr}=50000$ and leads to stable LES-CNN in all tests conducted here. Similarly, we use the ANN-based data-driven SGS model and the physics-based SGS model SMAG, DSMAG, and Mixed to conduct LES-ANN, LES-SMAG, LES-DSMAG, and LES-Mixed integrations. We also include results from LES-NM for reference in some figures.

Fig. 5 shows examples of the evolution of the kinetic energy $E(t) = \langle \overline{\psi} \overline{\omega} \rangle / 2$ of the 2D-DHIT flow from FDNS and from the different LES models for Re = 32000 as well as for Re = 8000. While the LES-CNN and LES-DSMAG are stable, LES-ANN is unstable, leading to rapid increases in E and blow up. In their pioneering work, Maulik et al. [71] also found this LES-ANN unstable and proposed a post-processing step:

$$\Pi_{i,j}^{\text{ANN}} = 0, \ \forall \ T_{i,j} < 0,$$
 (17)

which effectively, like the positive clipping used for DSMAG, eliminates backscattering based on *T* from Eq. (16). A similar procedure was used by Zhou et al. [140] to stabilize their LES-ANN for 3D-DHIT. While this post-processed LES-ANN is stable, it is excessively dissipative (even more than DSMAG) and substantially overpredicts the energy decay rate. LES-CNN, which is stable without any post-processing and accounts for both diffusion and backscattering, has the closest agreement with FDNS in terms of the decay rate. It should be pointed out that it is possible that increasing the number of training samples for the ANN also leads to a more accurate and perhaps a stable LES-ANN; however, as mentioned before, the focus of this work is on LES-CNN and a comprehensive investigation of LES-ANN is beyond the scope of this paper. We present the results with LES-DSMAG as a baseline and present the results with the recently published LES-ANN to give the readers a better view of the state-of-the-art in this field.

To examine the accuracy of LES-CNN in short-term forecasting, Fig. 6 presents the relative L_2 -norm error in the prediction of $\overline{\omega}$ averaged from 5 random initial conditions in the testing set from $t=50\tau$ to 200τ . The results show that LES-CNN has the highest accuracy, outperforming the next best model, DSMAG. The post-processed LES-ANN and LES-SMAG have substantially higher errors, which as the next analysis shows is due to their excessive dissipation. To further evaluate the

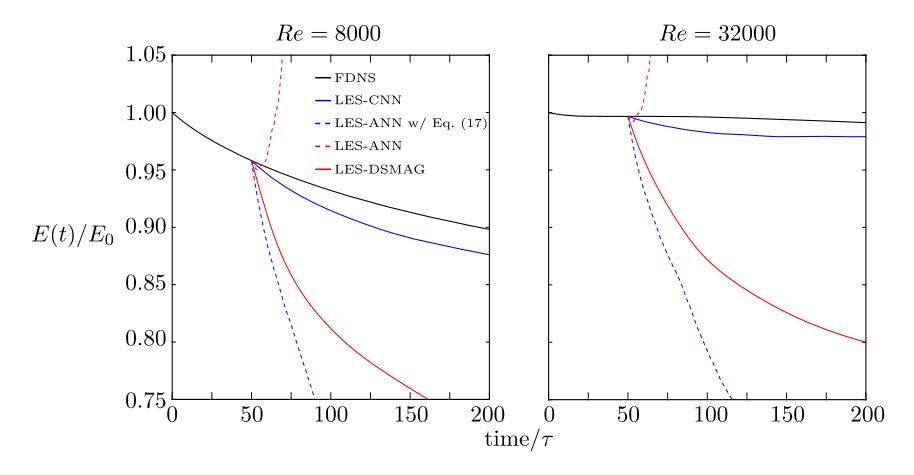


Fig. 5. Evolution of kinetic energy E(t) normalized by $E_0 = E(0)$ in a posteriori tests from 5 random initial conditions at Re = 8000 and Re = 32000. Note that for each Re, the ANN- and CNN-based data-driven SGS models have been trained on data from that Re. Curves show the mean from the 5 integrations. The LES integrations start at $t = 50\tau$. All stable LES models overpredict the decay rate but LES-CNN is closest to the FDNS while LES-DSMAG, and even more so the post-processed LES-ANN with backscattering removed, are too dissipative. LES-ANN without post-processing is unstable and blows up.

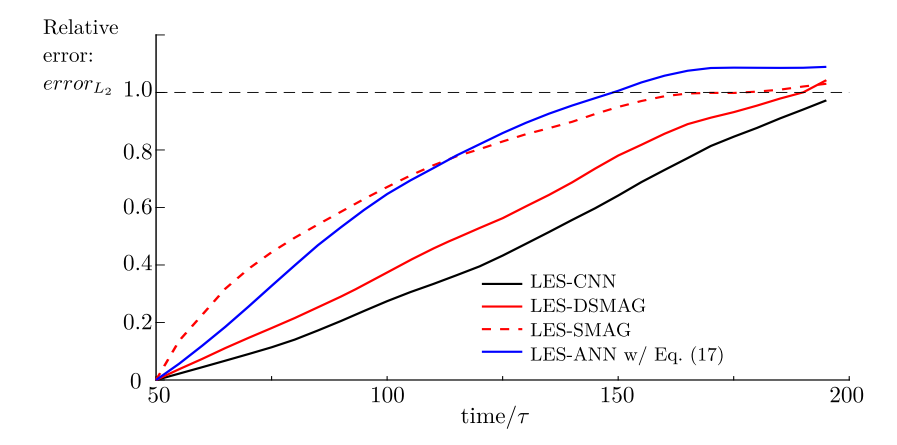


Fig. 6. Short-term prediction accuracy of LES models in *a posteriori* tests at Re = 32000. Predictions start at $t = 50\tau$ in the 5 testing sets. For each model, curves show the evolution of the relative L_2 -norm error, $error_{L_2}(t) = \|\bar{\omega}^{\text{LES}} - \bar{\omega}^{\text{FDNS}}\|_2 / \|\bar{\omega}^{\text{FDNS}}\|_2$, averaged over the 5 integrations. The LES-CNN has the highest accuracy and outperforms LES-DSMAG. The large error in the post-processed LES-ANN and in LES-SMAG is due to excessive dissipation (see Fig. 7).

short-term accuracy of these LES models, Fig. 7 shows an example of $\overline{\omega}(x,y)$ at $t=100\tau,150\tau$, and 200τ predicted from an initial condition at $t=50\tau$ in the testing set. Evidently, LES-CNN is capable of predicting both small- and large-scale structures well, and outperforms LES-DSMAG and LES-Mixed, which while capturing most of the large-scale structures well, misses many of the small-scale structures. The post-processed LES-ANN and LES-SMAG are too diffusive and miss most small-scale structures, substantially underpredicting the magnitude of $\overline{\omega}$, especially at later times. The LES-NM does not have any SGS transfer, and the molecular viscosity alone does not provide enough dissipation at this high Re, leading to substantial noise (unphysical high-wavenumber structures).

The above analysis shows that the superior accuracy of the CNN-based SGS model in *a priori* tests translates to high accuracy in short-term forecasts with LES-CNN in *a posteriori* tests. Next, we examine the accuracy of these *a posteriori* LES models in reproducing the statistics of the turbulent flow, which is an important test for the applicability of these models [78]. Fig. 8 shows the TKE spectrum and probability density function (PDF) of vorticity at $t = 200\tau$ from the 5 simulations in the testing sets. Among the LES models, LES-CNN has the best performance: its TKE spectrum matches that of the FDNS across wavenumbers and its PDF matches that of the FDNS, even at the end of the tails. The next best-performing model is LES-DSMAG, whose TKE spectrum overall agrees with FDNS, although this model is more diffusive than LES-CNN. The excessive diffusion is more noticeable in the PDF of the vorticity field: while the PDF of LES-DSMAG matches the bulk of the FDNS' PDF, there are large deviations at the tails, beyond ± 2 standard deviations. The post-processed LES-ANN with Eq. (17) and LES-SMAG are too diffusive, leading to TKE spectra that quickly curl down as k increases and PDFs that substantially deviate from the FDNS' PDF at the tails (for LES-SMAG, even in the bulk). Just to further demonstrate the importance of capturing backscattering in the outstanding performance of LES-CNN in matching the FDNS' spectrum and PDF, Fig. 8 also presents results from a post-processed LES-CNN with Eq. (17) (i.e., backscattering removed), showing that the model becomes excessively diffusive (with performance comparable to that of the LES-DSMAG). Due to the lack

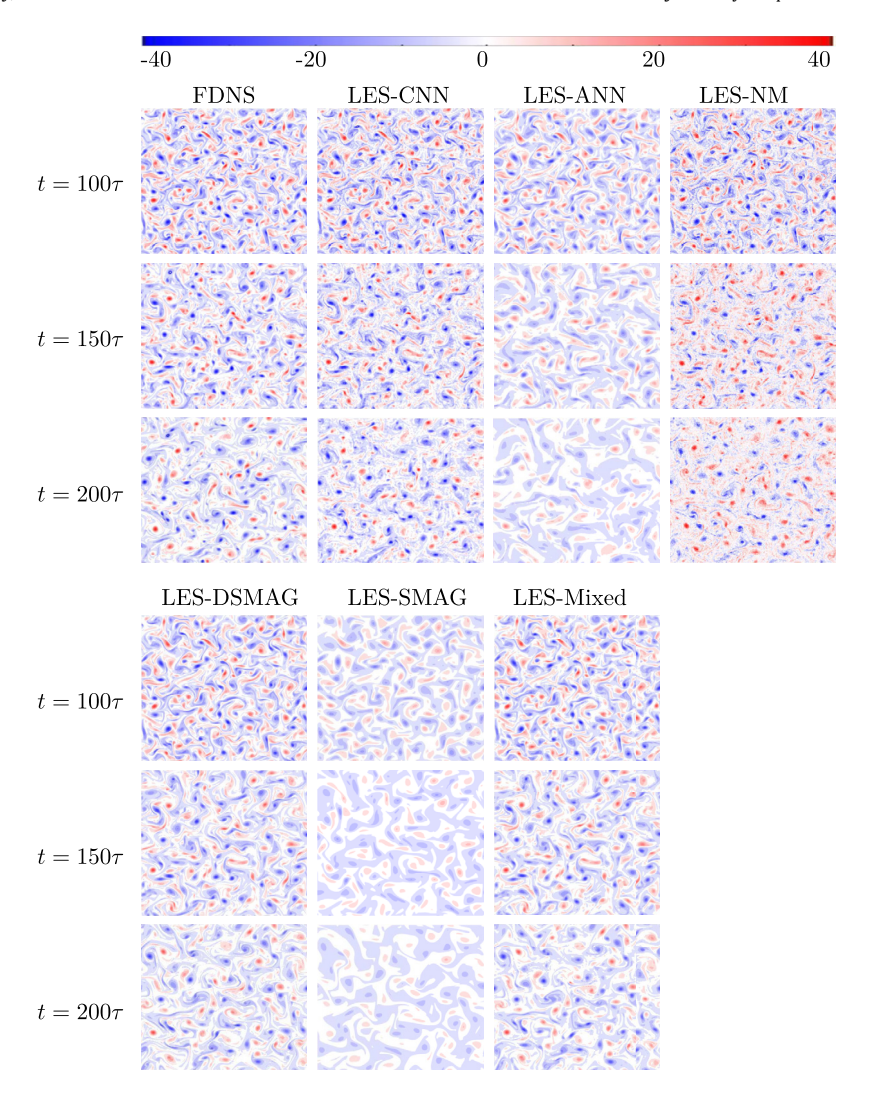


Fig. 7. Examples of the vorticity fields at $t=100\tau$, 150τ , and 200τ from one of the testing sets at Re=32000. $\overline{\omega}$ from FDNS is shown in the first row (used as the "truth" for the LES). The other panels show $\overline{\omega}$ predicted from $t=50\tau$ using 7 *a posteriori* LES models. The LES-CNN captures the patterns and magnitudes of both large- and small-scale structures well, except at the latest time at $t=200\tau$. While LES-DSMAG, and LES-Mixed predict most of the large-scale structures and some of the small-scale structures well, particularly at the earlier times, its overall accuracy is lower than that of LES-CNN (also see Fig. 6). The post-processed LES-ANN has a reasonably good performance at $t=100\tau$, but at later times, this model and the LES-SMAG model are too diffusive such that the magnitude of the vorticity field is underpredicted and small-scale structures are missing. The LES with no SGS model (LES-NM) results in excessive noise due to the lack of inter-scale dissipation.

of SGS dissipation, LES-NM results in unphysically high-wavenumber structures indicated by the curl-up at the end of the TKE spectrum and spuriously high extreme values of vorticity indicated by the large values at the tails of the PDF. The *a posteriori* results for Mixed are overall similar to LES-DSMAG (see Appendix C for more details).

The *a posteriori* results show the advantages of the CNN-based data-driven SGS model, which provides a stable LES model while capturing backscattering, and yields superior performance for both forecasting short-term spatio-temporal evolution and reproducing long-term statistics of the turbulent flow.

4.3. Transfer learning to higher Re

So far, we have tested the data-driven SGS model and the LES-CNN on flows with the same Re as the flow from which data was collected for the training of the CNN (Re = 8000 or Re = 32000). As discussed in the Introduction, the capability to generalize beyond the training flow, in particular to extrapolate to turbulent flows with higher Re in a posteriori tests, is essential for robust, trustworthy, and practically useful LES models. Neural networks are known to have difficulty with extrapolations, and in our recent work with multi-scale Lorenz 96 equations and forced 1D Burgers' turbulence, we found that data-driven SGS models do not generalize well to more chaotic systems or flows with $10 \times 10 \times 10^{-2}$ higher Re, leading to inaccurate predictions in a posteriori (online) tests [21,115]. Similarly, Fig. 9 shows that for the 2D-DHIT system studied here,

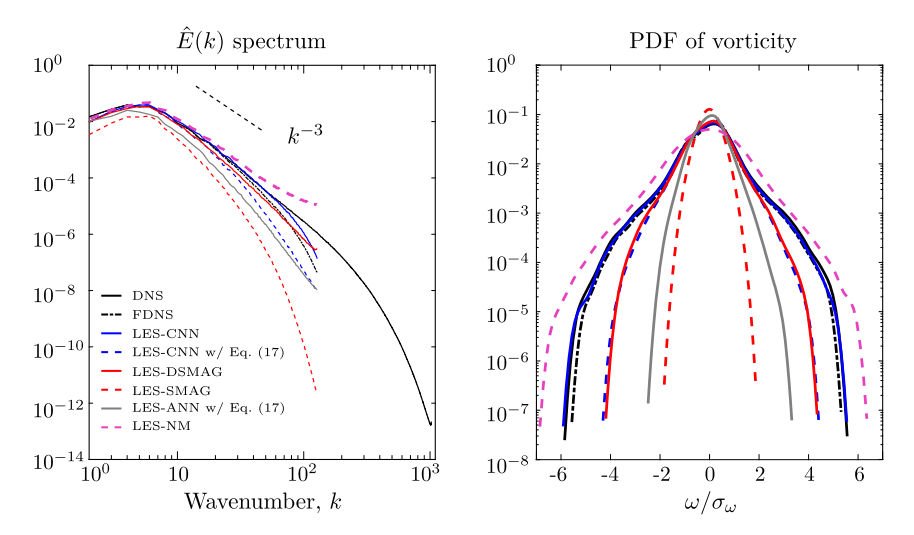


Fig. 8. The TKE spectrum $\hat{E}(k)$ and probability density function (PDF) of vorticity at $t=200\tau$ from a posteriori tests at Re=32000. Results are from independent runs in the 5 testing sets. For $\hat{E}(k)$, the spectrum from each run is calculated and then averaged. For the PDF, data from all 5 runs are combined and the PDF is calculated using a kernel estimator [126]. For both the TKE spectrum and PDF, the LES-CNN has the best performance, followed by LES-DSMAG. Results from post-processed LES-CNN with Eq. (17) are shown just to demonstrate the importance of capturing backscattering for the excellent performance of LES-CNN in reproducing the TKE spectrum of FDNS and the tails of the FDNS' PDF. The post-processed LES-ANN with Eq. (17) and LES-SMAG are too diffusive, which shows in both TKE spectrum and PDF. LES-NM does not have any SGS models, which leads to the appearance of high-wavenumber structures indicated by the curl-up in the TKE spectrum and the spuriously high extreme values of vorticity. See Fig. 14 for the results with LES-Mixed and LES-DSMAG without positive clipping.

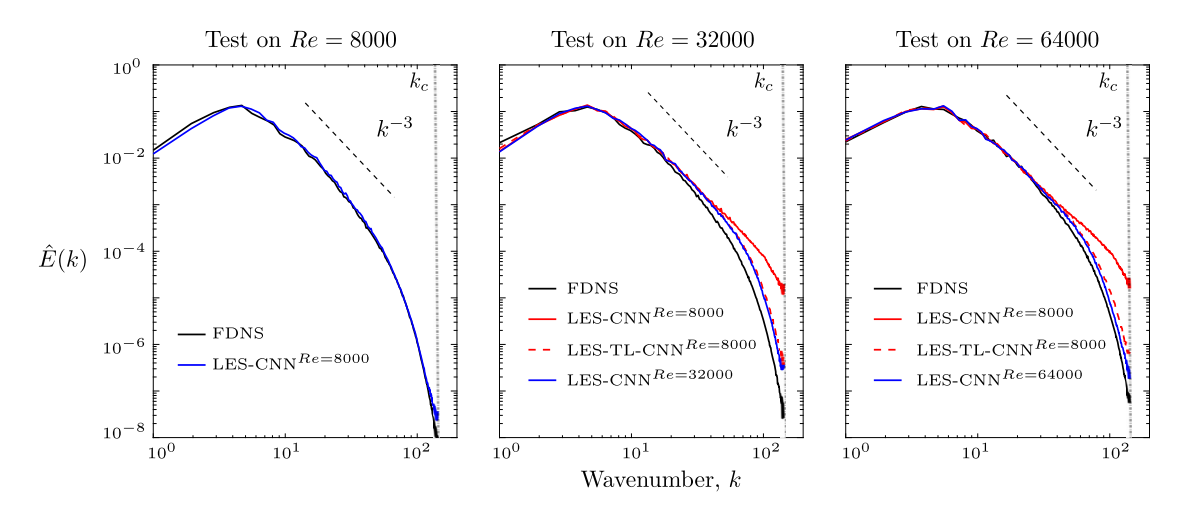


Fig. 9. Transfer learning to higher Re. The TKE spectrum $\hat{E}(k)$ at $t=200\tau$ from a posteriori tests at three different Re. Results are from independent runs in the 5 testing sets. For $\hat{E}(k)$, the spectrum from each run is calculated and then averaged. The superscript indicates the Re on which the CNN is trained with $n_{tr} = 5000$ samples. TL (transfer learned) means that the CNN has been re-trained with $n_{tr}^{TL} = 500$ samples (1% of n_{tr}) from the Re on which the LES-CNN is tested on (indicated in the title of each panel). In each panel, the blue lines show that the LES-CNN trained and tested on the same Re is accurate and its TKE spectrum agrees with that of the FDNS. However, the red lines in the two panels on the right show that the LES-CNN trained on Re = 8000 does not perform well at $4\times$ or $8\times$ higher Re, with the TKE spectra of the simulated flow substantially deviating from that of the FDNS at high k near k_c . The red dashed lines show that the LES-TL-CNN pre-trained on Re = 8000 and transfer learned with a small amount of data from the higher Re perform well at $4\times$ or $8\times$ higher Re.

a data-driven SGS model trained on data from Re = 8000 leads to a posteriori LES-CNN that is accurate only at Re = 8000 but not at Re = 32000 or 64000. At these higher Re, the TKE spectra deviate substantially from the spectrum of the FDNS. Note that currently, there is no well-established quantitative metric (of the training and testing data) to know whether the neural network needs to extrapolate or not, but as a first attempt to assess this in a priori analysis, one can evaluate the similarity between the training data and a set of testing data, for example, using the Mahalanobis distance [56,65] (see Appendix D).

In both Chattopadhyay et al. [21] and Subel et al. [115], we showed that transfer learning enables accurate generalization/extrapolation of data-driven SGS models to more chaotic systems and turbulent flows with a $10 \times$ higher Re, although the effectiveness of this approach beyond 1D and to more complex turbulent flows remained to be investigated.



Fig. 10. Schematic of the CNN with transfer learning for extrapolation to higher *Re*. Everything is the same as the original CNN shown in Fig. 3 with one exception: here, the first 8 Conv layers (gray) use the weights already computed during training with n_{tr} samples from the lower *Re* and are fixed (not to be trained). Only the last two Conv layers (blue) are going to be trained using $n_{tr}^{TL} = n_{tr}/100$ samples from the higher *Re*, after these layers are initialized not randomly but using the weights computed for the lower *Re*.

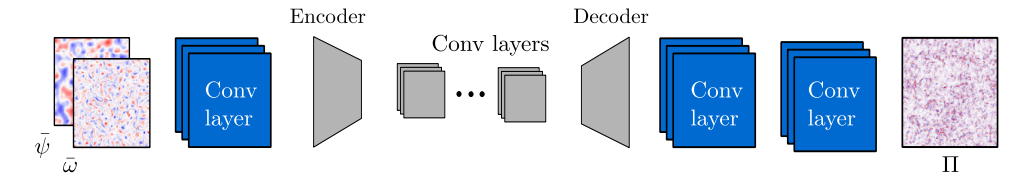


Fig. 11. Schematic of the CNN with transfer learning and encoder-decoder architecture for extrapolation to higher Re and higher LES grid resolution. There are few differences with the CNN shown in Fig. 10. Here, the input and output samples are at the higher resolution of 512^2 (inputs and outputs of the CNNs in Figs. 3 and 10 are at the resolution of 256^2). The 8 Conv layers that are already trained with n_{tr} samples from the lower Re and FDNS at the resolution of 256×256 are embedded within an encoder-decoder architecture. These 8 layers (gray) are fixed (not to be trained). The last two layers (in blue) are initialized not randomly but using the weights computed for the lower Re and lower resolution. A first layer (in blue) is added between the input and the encoder, and is initialized randomly. Only these three layers are going to be trained using $n_{tr}^{TL} = n_{tr}/100$ samples from the higher Re and higher resolution (512²).

Transfer learning involves taking a neural network that has been already trained for a given data distribution (e.g., flow with a given Re) using a large amount of data and re-training only some of its layers (usually the deeper layers) using a small amount of data from the new data distribution (e.g., flow with a higher Re) [38,136]. For example, Fig. 10 shows the schematic of the transfer-learned CNN used here. While similar to the original CNN (Fig. 3), there is one major difference: for transfer learning, the first 8 Conv layers use the weights already computed during training with n_{tr} samples from the lower Re. These weights are fixed and remain the same during the re-training. The last two Conv layers are initialized with weights computed during training with n_{tr} samples from the lower Re, but these two layers will be trained and their weights will be updated using $n_{tr}^{TL} = n_{tr}/100$ samples from the higher Re. The key idea of TL is that in deep neural networks, the first layers learn high-level features, and the low-level features that are specific to a particular data distribution are learned only in the deeper layers [38,136]. Therefore, for generalization, only the deeper layers need to be re-trained, which can be done using a small amount of data from the new distribution.

To examine the effectiveness of transfer learning in the 2D-DHIT testcase, we take the CNN that is already trained with n_{tr} samples from Re = 8000 and re-train it with $n_{tr}^{TL} = n_{tr}/100$ samples from the flow with Re = 32000 or Re = 64000. Fig. 9 shows that the a posteriori LES with these transfer-learned CNNs (LES-TL-CNN $^{Re=8000}$) accurately extrapolates to $4\times$ and $8\times Re$. In both cases, the accuracy of the transfer-learned LES-TL-CNN is as good as that of the LES-CNN trained with n_{tr} samples from Re = 32000 and Re = 64000. Before showing the results for accurate extrapolation to even higher Re ($16\times$) in the next section, we point out that the number of layers to be re-trained and the number of samples used for re-training (n_{tr}^{TL}) depend on the problem and require some trial and error for the best performance. Here, fixing the first 6 layers and re-training the deeper 4 layers (with the same n_{tr}^{TL}) leads to similar LES-TL-CNN performance. The goal of transfer learning is to minimize n_{tr}^{TL} while achieving the accuracy of n_{tr} , with the number of re-trained layers being a hyper-parameter to be tuned to achieve this goal. Substantial exploration in forced 1D Burgers' turbulence showed that the a posteriori performance of LES with transfer-learned data-driven SGS models mainly depends on n_{tr}^{TL} as long as more than one layer is re-trained [115].

4.4. Transfer learning to higher Re and higher LES numerical resolution

One often-cited disadvantage of using CNNs (compared to local ANNs) for data-driven SGS modeling is dependence on the specific LES resolution for which the CNN has been trained, limiting the use of the LES-CNN on a different grid resolution (and the use of transfer learning to extrapolate to even higher *Re* for which a higher LES resolution might be needed). Here, we show that this issue can be easily addressed by adding pooling (encoder) and upsampling (decoder) layers to the transfer learning architecture.

For example, to use a CNN-based data-driven SGS model trained on data from Re = 8000 and resolution 256×256 and conduct a posteriori LES-TL-CNN integrations at Re = 64000 or Re = 128000 with resolution $N_{LES} = 512$, we can use the encoder-decoder architecture shown in Fig. 11. Here, the number of convolutional layers are the same as before plus an additional layer before the encoder. The encoder with a pooling layer with stride two transforms the first layer from the input size (512×512) to the size of the layers of the CNN previously trained for a lower Re and resolution (256×256) . The

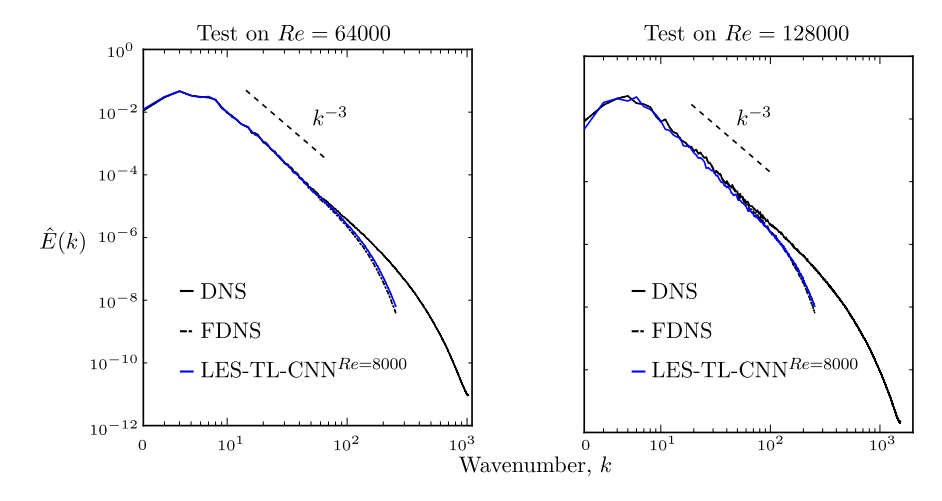


Fig. 12. Transfer learning to higher Re and higher LES numerical resolution. The TKE spectrum $\hat{E}(k)$ at $t=200\tau$ from a posteriori tests at two different Re. Results are from independent runs in the 5 testing sets. For $\hat{E}(k)$, the spectrum from each run is calculated and then averaged. The superscript indicates that the CNN has been trained with $n_{tr} = 50000$ samples from Re = 8000 at the resolution of 256 × 256. TL (transfer learned) means that the CNN has been re-trained with $n_{tr}^{TL} = 500$ samples (1% of n_{tr}) from the Re on which the LES-TL-CNN is tested on (indicated in the title of each panel) at the resolution of 512 × 512. In each panel, the spectra of the DNS and FDNS are shown; the latter is the "truth" for LES. Note that for Re = 64000, $N_{DNS} = 2048$ and for Re = 128000, $N_{DNS} = 3072$. The FDNS is at the resolution of 512². The blue lines show that the LES-TL-CNN pre-trained on Re = 8000 and transfer learned with a small amount of data from the higher Re and resolution perform well at 8× or 16× higher Re. Note that for LES-TL-CNN at both Re, here we use $N_{LES} = 512$.

8 layers within the encoder-decoder have the weights already computed during training with n_{tr} samples from the lower Re. These weights are kept fixed and these layers are not going to be trained. A decoder transforms the output of the last of these layers from the size 256×256 to the size of the first of the last two layers, which is 512×512 . Similar to Fig. 10, these two final layers are initialized with weights computed during training with n_{tr} samples from the lower Re (and lower resolution). Only these two layers and the very first layer will be trained and their weights are updated using $n_{tr}^{TL} = n_{tr}/100$ samples from the higher Re and higher resolution. Here we use a factor of two increase in the resolution in each direction just as an example, and this approach can be used on any other resolution changes too.

Fig. 12 shows, for Re = 64000 and Re = 128000, the TKE spectrum for LES-TL-CNN in comparison to that of FDNS. In this LES-TL-CNN, the numerical resolution is $N_{\rm LES} \times N_{\rm LES} = 512 \times 512$ and its CNN has been trained with $n_{tr} = 50000$ samples from Re = 8000 with resolution 256^2 and transfer-learned with $n_{tr}^{TL} = n_{tr}/100$ samples from Re = 64000 or Re = 128000 at the resolution of 512^2 . The results show that transfer learning enables extrapolation to over an order-of-magnitude increase in Re (16×) and with the encoder-decoder architecture, enables transfer between different LES resolutions. The implications of these findings, in particular for practical purposes, are discussed in the next section.

5. Summary and future directions

Using 2D decaying turbulence as the testbed, we have examined the performance of a CNN-based, non-local, data-driven SGS model in *a priori* and *a posteriori* analyses, with training and testing done on data from flows with the same *Re*. We have also investigated the effectiveness of transfer learning in enabling *a posteriori* LES-CNNs that are trained on data from flows with low *Re* (and low grid resolution) to work for flows with higher *Re* (and higher grid resolution). In all cases, training is done on filtered DNS data, and the performance is tested in comparison with out-of-sample filtered DNS data.

As discussed in Section 4.1, a priori tests at Re = 32000 show that the trained data-driven SGS model can accurately predict the SGS forcing terms from never-seen-before snapshots of the resolved flow with correlation coefficients c (Eq. (15)) around 0.93, substantially outperforming the baseline physics-based SGS models, DSMAG, and Mixed. The data-driven SGS model is also found to accurately capture both forward transfer and backscattering between the resolved and unresolved scales.

To examine the connection between *a priori* and *a posteriori* performance, we have evaluated the accuracy of *a priori* tests (in terms of *c*) and the stability of *a posteriori* LES-CNN as the number of training samples are varied from $n_{tr} = 500$ to 50000 (Table 2). This analysis shows that while the SGS model trained with $n_{tr} = 10000$ seems accurate (with c = 0.90), the LES with this CNN (and CNNs trained with smaller n_{tr}) is not stable. Increasing n_{tr} to 30000 and 50000 further improves c to 0.92 and 0.93, respectively, and leads to accurate and stable *a posteriori* LES-CNN, without any need for post-processing or additional eddy viscosity. More analysis, in which c is calculated separately for grid points experiencing only forward transfer or only backscattering, shows that at low n_{tr} , the CNN captures backscattering with much lower accuracy compared to forward transfer, but that the difference decreases as n_{tr} is increased. This analysis suggests that the instabilities of *a posteriori* LES-CNN trained with small training sets might be due to the inability of the SGS model to

correctly represent backscattering. Why learning backscattering requires more data remains to be studied in future work. This might be because backscattering is fundamentally harder to learn data drivenly, or because backscattering is less frequent than forward transfer, or both. While we do not claim that all instabilities in *a posteriori* (online) tests are due to this issue and could be overcome by increasing n_{tr} , we believe that these findings can help future studies in understanding the reasons(s) behind these instabilities and formulating rigorous solutions (see below for further discussions).

As discussed in Section 4.2, a posteriori tests at Re=32000 with the CNN trained with $n_{tr}=50000$ show that LES-CNN is stable and accurate. The LES-CNN outperforms LES-DSMAG and LES with other tested SGS models in terms of both short-term forecast and re-producing the TKE spectrum and PDF of vorticity (even at the tails). The main shortcoming of the other models is that they are too diffusive, primarily because they do not capture backscattering due to their formulation or post-processing steps used to make them stable. The CNN-based SGS model learns both forward transfer and backscattering non-parametrically from data, and as mentioned above, once the latter is accurately captured with enough training samples, this SGS model leads to an accurate and stable *a posteriori* LES-CNN.

The analysis presented in Section 4.3 shows that a data-driven SGS model trained at Re = 8000 does not lead to accurate a posteriori LES-CNN solutions (in terms of TKE spectra) at the higher Re, e.g., at Re = 32000 or Re = 64000. However, we show that transfer learning largely solves this problem and enables the LES-CNN trained for a flow at low Re to provide accurate and stable solutions for flows with higher Re while requiring only a small amount of data from the flow at higher Re. The data-driven SGS model can even be coupled with LES solvers that use higher grid resolutions by adding an encoder-decoder architecture to the transfer-learned CNN (Section 4.4). For example, we show that a CNN trained with $n_{tr} = 50000$ samples from Re = 8000 (at filtered resolution 256×256) can provide an accurate and stable a posteriori LES-CNN for flows with Re = 128000 and $N_{LES} = 512$ once 2 out of the 10 convolution layers of the CNN are re-trained with only $n_{tr}^{TL} = n_{tr}/100 = 500$ samples from Re = 128000. To the best of our knowledge, this is the first application of transfer learning to building generalizable data-driven SGS models beyond 1D turbulence (the 1D results were presented in our recent work [115]).

In summary, in a canonical 2D turbulent flow, we present promising results that CNNs and transfer learning can be used together to build non-local data-driven SGS models that lead to accurate, stable, and generalizable LES models. The generalization capability provided by transfer learning is key in making such data-driven SGS models practically useful. This is because training a base CNN model with a large training set of high-fidelity data from low Re and then requiring only a small amount of high-fidelity data from the higher Re for re-training is highly desirable for turbulence modeling, given the sharp increase in the computational cost of high-fidelity simulations such as DNS for higher Re. It should be also highlighted that because transfer learning only requires a small amount of data and re-training only a few layers, its training process is fast and has a low computational cost, thus it can be conducted on the fly, for example when dealing with non-stationary systems. Moreover, the ability to also transfer between different LES resolutions further broadens the applicability of non-local SGS models. While not examined here, it is also possible that transfer learning provides generalization beyond Re and grid resolution, for example between canonical fluid systems and fluid flows with more complex geometries. Such applications should be explored in future work.

Beyond the obvious need to study the performance of the CNN-based SGS models and transfer learning in more complex turbulent flows (e.g., 3D, wall turbulence, stratified), there are a number of avenues to pursue in order to further expand and improve the methodology. The number of training samples might be potentially reduced, without loss of accuracy or stability, using data augmentation, e.g., through pre-processing the training data by exploiting the symmetries in the flow [84,115], and/or using physics-informed ML [47]. Examples of the latter include adding components (such as capsules [20] and transformers [19]) that better preserve spatial correlations in the CNN or imposing physical constraints in the loss function [e.g., 47,128]. Establishing a connection between accuracy in a priori tests and stability in a posteriori tests would also be substantially helpful. Note that in this work (and in most other SGS modeling studies), an "offline training" strategy is used: the SGS model is first trained using snapshots of the resolved flow as inputs and snapshots of the SGS term as outputs, and then this trained data-driven model is coupled with the coarse-resolution LES solver. At least some of the issues related to stability could be potentially resolved, and even scaling with the size of training set could be improved, by using an "online training" strategy, which involves training the data-driven model to find the best SGS term that evolves the solution of the LES closest to that of the DNS. Sirignano et al. [110] have recently presented an exciting and promising framework for such an approach. Exploring data-driven SGS models that account for non-Markovian effects arising from coarse-graining, as suggested by the Mori-Zwanzig formalism [22,62,87,127], is another direction to pursue in future work. Finally, interpreting the CNNs that provide accurate SGS models, such as the one trained here, can lead to insight into the SGS physics and possibly even better data-driven and/or physics-based models. While interpreting neural networks is currently challenging, using them along with data-driven equation discovery methods might provide a stepping stone, as for example done for ocean mesoscale eddies in pioneering work by Zanna and Bolton [138].

CRediT authorship contribution statement

Yifei Guan: Conceptualization, Methodology, Investigation, Validation, Formal analysis, Data curation, Visualization, Writing – original draft; Ashesh Chattopadhyay: Investigation, Validation, Writing; Adam Subel: Investigation, Validation, Writing; Pedram Hassanzadeh: Conceptualization, Supervision, Writing – review & editing, Funding acquisition.

Declaration of competing interest

The authors declare that they have no known competing financial interests or personal relationships that could have appeared to influence the work reported in this paper.

Acknowledgments

We thank Romit Maulik, Tapio Schneider, and Laure Zanna for insightful discussions about data-driven SGS modeling, and Karan Jakhar, Rambod Mojgani, and Ebrahim Nabizadeh for helpful comments on the manuscript. This work was supported by an award from the ONR Young Investigator Program (N00014-20-1-2722) and a grant from the NSF CSSI program (OAC-2005123) to P.H. Computational resources were provided by NSF XSEDE (allocation ATM170020) to use Bridges GPU and Comet GPU clusters and by the Rice University Center for Research Computing. The codes for CNN and CNN with transfer learning are publicly available at https://github.com/envfluids/2D-DDP.

Appendix A. Initial condition for DNS

Following previous studies, we choose the initial conditions of DNS to have the same energy spectrum but randomly different vorticity fields [70,71,82]. The initial energy spectrum is given by [82]

$$\hat{E}(k) = Ak^4 e^{-(k/k_p)^2},\tag{18}$$

where the amplitude is

$$A = \frac{4k_p^{-5}}{3\pi},\tag{19}$$

and $k = |\mathbf{k}| = \sqrt{k_x^2 + k_y^2}$. The maximum value of the energy spectrum occurs at $\sqrt{2}k_p$, where $k_p = 10$ is used here following Ref. [70]. The given energy spectrum in turn determines the magnitude of the Fourier coefficients of vorticity:

$$|\hat{\omega}(\mathbf{k})| = \sqrt{\frac{k}{\pi}} \hat{E}(k). \tag{20}$$

Then the vorticity distribution in Fourier space is

$$\hat{\omega}(\mathbf{k}) = |\hat{\omega}(\mathbf{k})|e^{\mathbf{i}\eta(\mathbf{k})},\tag{21}$$

where $\eta(\mathbf{k}) = \eta_1(\mathbf{k}) + \eta_2(\mathbf{k})$. $\eta_1(\mathbf{k})$ and $\eta_2(\mathbf{k})$ are independent random numbers from a uniform distribution in $[0, 2\pi]$ at each (k_x, k_y) when both $k_x, k_y \ge 0$ (first quadrant of the $k_x - k_y$ plane). The values at the other quadrants are as follows:

$$\eta(\mathbf{k}) = -\eta_1(\mathbf{k}) + \eta_2(\mathbf{k}) \text{ for } k_x < 0, k_y > 0$$
(22a)

$$\eta(\mathbf{k}) = -\eta_1(\mathbf{k}) - \eta_2(\mathbf{k}) \text{ for } k_x < 0, k_y < 0$$
(22b)

$$\eta(\mathbf{k}) = +\eta_1(\mathbf{k}) - \eta_2(\mathbf{k}) \text{ for } k_x \ge 0, k_y < 0$$
(22c)

The initial vorticity field is applied at t = 0.

Figs. 1(a) and 1(d) show an example of the initial $\omega(x,y)$ and the corresponding $\hat{E}(k)$, respectively. The initial vorticity is dominated by relatively large-scale structures, but small-scale structures emerge as the flow evolves (Figs. 1(b), (c), and (d)). From $t \approx 50\tau$, the $\hat{E}(k)$ spectrum exhibits self-similarity and follows the Kraichnan-Batchelor-Leith (KBL) theory [6,52,58]. Between $t = 50\tau$ and 200τ , the flow decays due to the viscous dissipation, the small-scale structures fade away, and the large, coherent vortices merge and grow as a result of the inverse energy cascade. Following previous studies, we focus on this phase of the decaying 2D turbulence and discard the first 50τ as spin-up [7,70].

Appendix B. A posteriori results for LES-CNN with smaller training set ($n_{tr} = 10000$)

Fig. 13 shows the TKE spectra and PDF of vorticity for LES-CNN with $n_{tr} = 10000$ compared to DNS, FDNS, and LES-CNN with $n_{tr} = 50000$. Without enough training data, LES-CNN ($n_{tr} = 10000$) overpredicts the TKE of the high wavenumbers and therefore leads to unphysically values of vorticity (spuriously large values of the PDF). See Table 2 for *a priori* results.

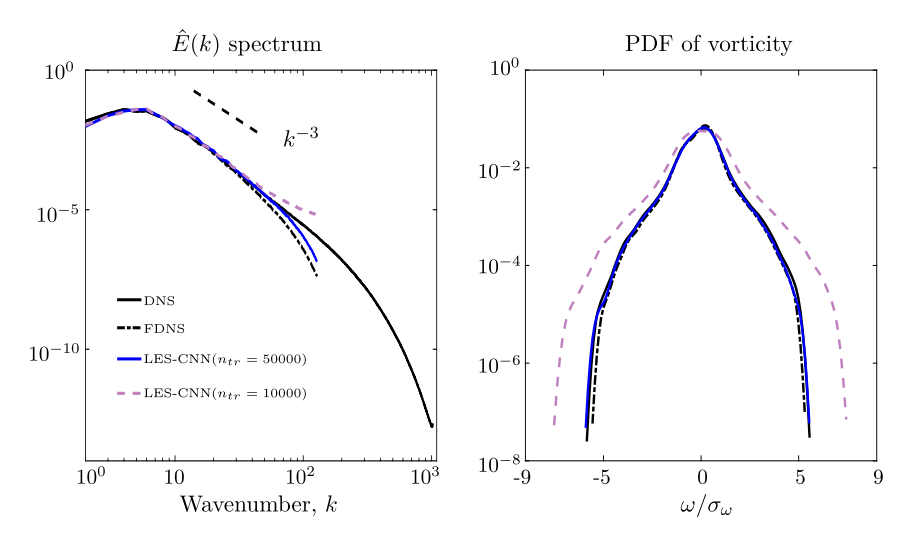


Fig. 13. Same as Fig. 8 but for LES-CNN ($n_{tr} = 10000$) compared to LES-CNN ($n_{tr} = 50000$, the one used in other *a posteriori* analyses) and DNS and FDNS. Results from LES-CNN ($n_{tr} = 10000$) demonstrate the importance of the size of the training set to achieve stable and accurate *a posteriori* LES.

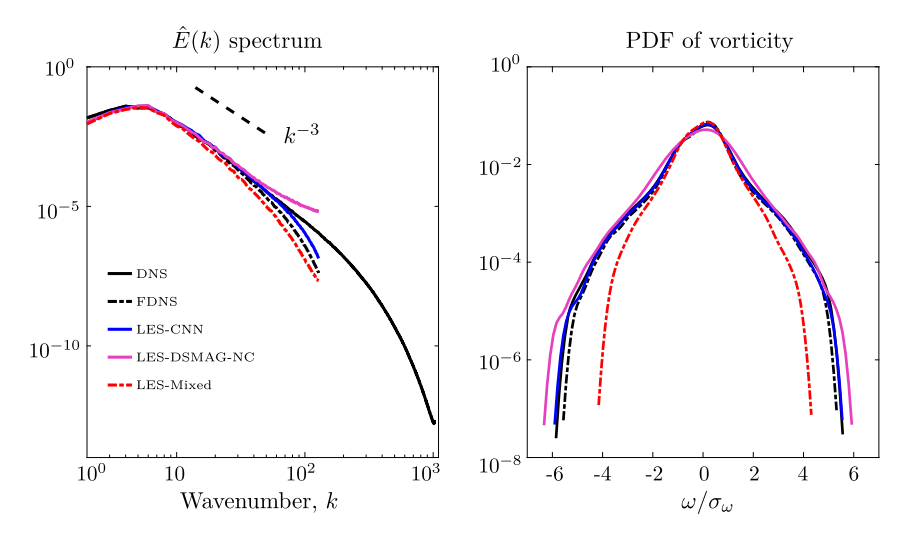


Fig. 14. Same as Fig. 8 but for LES-Mixed and LES-DSMAG-NC (no positive clipping) compared to LES-CNN (and DNS and FDNS). For both the TKE spectrum and PDF, the LES-CNN outperforms LES-Mixed, which allows backscattering. Results from LES-DSMAG-NC demonstrate the importance of capturing interscale transfer in reproducing the FDNS' TKE spectrum the tails of the PDF.

Appendix C. A posteriori results for LES-DSMAG without clipping and LES-Mixed

Fig. 14 shows the TKE spectra and PDF of vorticity for LES-DSMAG without positive clipping (LES-DSMAG-NC) and LES-Mixed compared to DNS, FDNS, and LES-CNN. LES-DSMAG-NC follows the same procedure as the LES-DSMAG except that it allows negative eddy viscosity to represent backscattering (anti-diffusion). As the eddy viscosity is uniform over the computational domain at each time step, $\Pi^{DSMAG-NC}$ can be either purely diffusive (same as Π^{DSMAG}) or purely anti-diffusive. LES-DSMAG-NC overpredicts the TKE of the high wavenumbers and therefore leads to unphysically extreme values of vorticity (the tail of the PDF). On the other hand, LES-Mixed underpredicts the TKE over a broad range of wavenumbers starting from the inertial range, and therefore, the vorticity values are smaller than the ones produced by DNS, FDNS, and LES-CNN.

Appendix D. Mahalanobis distance between the training data and new testing data as a function of Re

We compute the similarity between the training data and a set of testing data using the Mahalanobis distance \mathcal{D} [56,65]:

$$\mathcal{D} = \max \left[\sqrt{(\mathbf{u} - \mu)^T \Sigma^{-1} (\mathbf{u} - \mu)} \right], \tag{23}$$

where $\mathbf{u} = [\bar{\psi}, \bar{\omega}]$ or $\mathbf{u} = [\Pi]$ for input or output data similarity evaluation, respectively. μ is the mean and Σ is the covariance matrix of the *original training data* distribution (e.g., at Re = 8000 in this work). If \mathcal{D} computed for \mathbf{u} from the

new testing data (e.g., data at higher Re) is large, it indicates that the new testing data likely lie outside the range of the original training data distribution (at Re=8000), requiring the CNN to extrapolate. Here we define $\mathcal R$ as the standardized ratio of $\mathcal D$ of output (or input) at high Re to $\mathcal D$ at Re=8000: $\mathcal R_{Re}=\mathcal D_{Re}/\mathcal D_{Re=8000}$. We have found that for the output Π , $\mathcal R_{Re=32000}=2$, $\mathcal R_{Re=64000}=2.5$, and $\mathcal R_{Re=128000}=3$, while $\mathcal R=1.1-1.2$ for inputs for all cases (the small change in $\mathcal D$ for input is due to the decaying nature of the flow here). This analysis suggests that extrapolation is needed for $\mathcal R$ as small as 2. Future work should comprehensively explore the relationship between $\mathcal R$, c (correlation coefficient), and some measure of the quality of the a posteriori analysis for different Re and test cases.

References

- [1] A. Arakawa, V.R. Lamb, Computational design of the basic dynamical processes of the UCLA general circulation model, in: General Circulation Models of the Atmosphere 17 (Supplement C) (1977) 173–265.
- [2] H. Arbabi, I. Mezić, Study of dynamics in post-transient flows using Koopman mode decomposition, Phys. Rev. Fluids 2 (12) (2017) 124402.
- [3] Y. Bar-Sinai, S. Hoyer, J. Hickey, M.P. Brenner, Learning data-driven discretizations for partial differential equations, Proc. Natl. Acad. Sci. 116 (31) (2019) 15344–15349.
- [4] J. Bardina, J. Ferziger, W. Reynolds, Improved subgrid-scale models for large-eddy simulation, in: 13th Fluid and Plasmadynamics Conference, 1980, p. 1357.
- [5] J.A. Barranco, P.S. Marcus, A 3D spectral anelastic hydrodynamic code for shearing, stratified flows, J. Comput. Phys. 219 (1) (2006) 21-46.
- [6] G.K. Batchelor, Computation of the energy spectrum in homogeneous two-dimensional turbulence, Phys. Fluids 12 (12) (1969) II-233.
- [7] A. Beck, D. Flad, C.-D. Munz, Deep neural networks for data-driven LES closure models, I. Comput. Phys. 398 (2019) 108910.
- [8] A. Beck, M. Kurz, A perspective on machine learning methods in turbulence modelling, arXiv preprint, arXiv:2010.12226, 2020.
- [9] J. Berner, F. Doblas-Reyes, T. Palmer, G. Shutts, A. Weisheimer, Impact of a quasi-stochastic cellular automaton backscatter scheme on the systematic error and seasonal prediction skill of a global climate model, Philos. Trans. R. Soc. A, Math. Phys. Eng. Sci. 366 (1875) (2008) 2559–2577.
- [10] G. Boffetta, S. Musacchio, Evidence for the double cascade scenario in two-dimensional turbulence, Phys. Rev. E 82 (1) (2010) 016307.
- [11] T. Bolton, L. Zanna, Applications of deep learning to ocean data inference and subgrid parameterization, J. Adv. Model. Earth Syst. 11 (1) (2019) 376–399.
- [12] J.P. Boyd, Chebyshev and Fourier Spectral Methods, Courier Corporation, 2001.
- [13] S.L. Brunton, B.R. Noack, P. Koumoutsakos, Machine learning for fluid mechanics, Annu. Rev. Fluid Mech. 52 (2020) 477-508.
- [14] D. Carati, S. Ghosal, P. Moin, On the representation of backscatter in dynamic localization models, Phys. Fluids 7 (3) (1995) 606-616.
- [15] G.J. Chandler, R.R. Kerswell, Invariant recurrent solutions embedded in a turbulent two-dimensional Kolmogorov flow, J. Fluid Mech. 722 (2013) 554–595
- [16] J.R. Chasnov, Simulation of the Kolmogorov inertial subrange using an improved subgrid model, Phys. Fluids A, Fluid Dyn. 3 (1) (1991) 188-200.
- [17] A. Chattopadhyay, P. Hassanzadeh, S. Pasha, Predicting clustered weather patterns: a test case for applications of convolutional neural networks to spatio-temporal climate data, Sci. Rep. 10 (1) (2020) 1–13.
- [18] A. Chattopadhyay, P. Hassanzadeh, D. Subramanian, Data-driven predictions of a multiscale Lorenz 96 chaotic system using machine-learning methods: reservoir computing, artificial neural network, and long short-term memory network, Nonlinear Process. Geophys. 27 (3) (2020) 373–389.
- [19] A. Chattopadhyay, M. Mustafa, P. Hassanzadeh, K. Kashinath, Deep spatial transformers for autoregressive data-driven forecasting of geophysical turbulence, in: Proceedings of the 10th International Conference on Climate Informatics, 2020, pp. 106–112.
- [20] A. Chattopadhyay, E. Nabizadeh, P. Hassanzadeh, Analog forecasting of extreme-causing weather patterns using deep learning, J. Adv. Model. Earth Syst. 12 (2) (2020) e2019MS001958.
- [21] A. Chattopadhyay, A. Subel, P. Hassanzadeh, Data-driven super-parameterization using deep learning: experimentation with multi-scale Lorenz 96 systems and transfer-learning, J. Adv. Model. Earth Syst. 12 (11) (2020) e2020MS002084.
- [22] A.J. Chorin, O.H. Hald, R. Kupferman, Optimal prediction and the Mori–Zwanzig representation of irreversible processes, Proc. Natl. Acad. Sci. 97 (7) (2000) 2968–2973.
- [23] R.A. Clark, J.H. Ferziger, W.C. Reynolds, Evaluation of subgrid-scale models using an accurately simulated turbulent flow, J. Fluid Mech. 91 (1) (1979)
- [24] A. Dipankar, B. Stevens, R. Heinze, C. Moseley, G. Zängl, M. Giorgetta, S. Brdar, Large eddy simulation using the general circulation model ICON, J. Adv. Model. Earth Syst. 7 (3) (2015) 963–986.
- [25] J.A. Domaradzki, R.W. Metcalfe, R.S. Rogallo, J.J. Riley, Analysis of subgrid-scale eddy viscosity with use of results from direct numerical simulations, Phys. Rev. Lett. 58 (6) (1987) 547.
- [26] J.A. Domaradzki, E.M. Saiki, A subgrid-scale model based on the estimation of unresolved scales of turbulence, Phys. Fluids 9 (7) (1997) 2148-2164.
- [27] S.B. Driss, M. Soua, R. Kachouri, M. Akil, A comparison study between MLP and convolutional neural network models for character recognition, in: Real-Time Image and Video Processing 2017, vol. 10223, International Society for Optics and Photonics, 2017.
- [28] O.R. Dunbar, A. Garbuno-Inigo, T. Schneider, A.M. Stuart, Calibration and uncertainty quantification of convective parameters in an idealized GCM, arXiv preprint, arXiv:2012.13262, 2020.
- [29] K. Duraisamy, Machine learning-augmented Reynolds-averaged and large eddy simulation models of turbulence, arXiv preprint, arXiv:2009.10675, 2020
- [30] K. Duraisamy, G. Iaccarino, H. Xiao, Turbulence modeling in the age of data, Annu. Rev. Fluid Mech. 51 (2019) 357-377.
- [31] V. Eswaran, S.B. Pope, An examination of forcing in direct numerical simulations of turbulence, Comput. Fluids 16 (3) (1988) 257-278.
- [32] S. Formentin, M. Mazzoleni, M. Scandella, F. Previdi, Nonlinear system identification via data augmentation, Syst. Control Lett. 128 (2019) 56-63.
- [33] R.O. Fox, Large-eddy-simulation tools for multiphase flows, Annu. Rev. Fluid Mech. 44 (2012) 47-76.
- [34] B. Fox-Kemper, D. Menemenlis, Can large eddy simulation techniques improve mesoscale rich ocean models, in: Ocean Modeling in an Eddying Regime, vol. 177, 2008, pp. 319–337.
- [35] H. Frezat, G. Balarac, J.L. Sommer, R. Fablet, R. Lguensat, Physical invariance in neural networks for subgrid-scale scalar flux modeling, arXiv preprint, arXiv:2010.04663, 2020.
- [36] M. Gamahara, Y. Hattori, Searching for turbulence models by artificial neural network, Phys. Rev. Fluids 2 (5) (2017) 054604.
- [37] M. Germano, U. Piomelli, P. Moin, W.H. Cabot, A dynamic subgrid-scale eddy viscosity model, Phys. Fluids A, Fluid Dyn. 3 (7) (1991) 1760-1765.
- [38] I. Goodfellow, Y. Bengio, A. Courville, Y. Bengio, Deep Learning, vol. 1, MIT Press, Cambridge, 2016.
- [39] I. Grooms, Y. Lee, A.J. Majda, Numerical schemes for stochastic backscatter in the inverse cascade of quasigeostrophic turbulence, Multiscale Model. Simul. 13 (3) (2015) 1001–1021.
- [40] A.P. Guillaumin, L. Zanna, Stochastic-deep learning parameterization of ocean momentum forcing, J. Adv. Model. Earth Syst. 13 (9) (2021) e2021MS002534.

- [41] P. Hassanzadeh, P.S. Marcus, P. Le Gal, The universal aspect ratio of vortices in rotating stratified flows: theory and simulation, J. Fluid Mech. 706 (2012) 46–57.
- [42] H.T. Hewitt, M. Roberts, P. Mathiot, A. Biastoch, E. Blockley, E.P. Chassignet, B. Fox-Kemper, P. Hyder, D.P. Marshall, E. Popova, et al., Resolving and parameterising the ocean mesoscale in earth system models, Curr. Clim. Change Rep. (2020) 1–16.
- [43] M.F. Jansen, I.M. Held, Parameterizing subgrid-scale eddy effects using energetically consistent backscatter, Ocean Model. 80 (2014) 36-48.
- [44] M.F. Jansen, I.M. Held, A. Adcroft, R. Hallberg, Energy budget-based backscatter in an eddy permitting primitive equation model, Ocean Model. 94 (2015) 15–26.
- 1451 I. liménez, Transition to turbulence in two-dimensional Poiseuille flow, J. Fluid Mech. 218 (1990) 265–297.
- [46] M.L. Kaandorp, R.P. Dwight, Data-driven modelling of the Reynolds stress tensor using random forests with invariance, Comput. Fluids (2020) 104497.
- [47] K. Kashinath, M. Mustafa, A. Albert, J.-L. Wu, C. Jiang, S. Esmaeilzadeh, K. Azizzadenesheli, R. Wang, A. Chattopadhyay, A. Singh, A. Manepalli, D. Chirila, R. Yu, R. Walters, B. White, H. Xiao, H.A. Tchelepi, P. Marcus, A. Anandkumar, P. Hassanzadeh, Prabhat, Physics-informed machine learning: case studies for weather and climate modelling, Philos. Trans. R. Soc. A, Math. Phys. Eng. Sci. 379 (2194) (2021) 20200093.
- [48] R.M. Kerr, J.A. Domaradzki, G. Barbier, Small-scale properties of nonlinear interactions and subgrid-scale energy transfer in isotropic turbulence, Phys. Fluids 8 (1) (1996) 197–208.
- [49] S. Khani, M.L. Waite, Backscatter in stratified turbulence, Eur. J. Mech. B, Fluids 60 (2016) 1-12.
- [50] M.A. Khodkar, P. Hassanzadeh, S. Nabi, P. Grover, Reduced-order modeling of fully turbulent buoyancy-driven flows using the Green's function method, Phys. Rev. Fluids 4 (1) (2019) 013801.
- [51] B. Knaepen, P. Moin, Large-eddy simulation of conductive flows at low magnetic Reynolds number, Phys. Fluids 16 (5) (2004) 1255-1261.
- [52] R.H. Kraichnan, Inertial ranges in two-dimensional turbulence, Phys. Fluids 10 (7) (1967) 1417-1423.
- [53] A. Krizhevsky, I. Sutskever, G.E. Hinton, Imagenet classification with deep convolutional neural networks, in: Advances in Neural Information Processing Systems, 2012, pp. 1097–1105.
- [54] D. Krueger, E. Caballero, J.-H. Jacobsen, A. Zhang, J. Binas, R.L. Priol, A. Courville, Out-of-distribution generalization via risk extrapolation (REx), arXiv preprint, arXiv:2003.00688, 2020.
- [55] M. Kurz, A. Beck, A machine learning framework for LES closure terms, arXiv preprint, arXiv:2010.03030, 2020.
- [56] M. Kurz, A. Beck, Investigating model-data inconsistency in data-informed turbulence closure terms, in: 14th WCCM-ECCOMAS Congress 2020, vol. 1700, 2021.
- [57] Y. LeCun, B.E. Boser, J.S. Denker, D. Henderson, R.E. Howard, W.E. Hubbard, L.D. Jackel, Handwritten digit recognition with a back-propagation network, in: Advances in Neural Information Processing Systems, 1990, pp. 396–404.
- [58] C. Leith, Atmospheric predictability and two-dimensional turbulence, J. Atmos. Sci. 28 (2) (1971) 145-161.
- [59] A. Leonard, Energy cascade in large-eddy simulations of turbulent fluid flows, in: Advances in Geophysics, vol. 18, Elsevier, 1975, pp. 237-248.
- [60] A. Leonard, A. Leonard, Large-eddy simulation of chaotic convection and beyond, in: 35th Aerospace Sciences Meeting and Exhibit, 1997, p. 204.
- [61] D. Leslie, G. Quarini, The application of turbulence theory to the formulation of subgrid modelling procedures, J. Fluid Mech. 91 (1) (1979) 65-91.
- [62] Z. Li, X. Bian, X. Li, G.E. Karniadakis, Incorporation of memory effects in coarse-grained modeling via the Mori-Zwanzig formalism, J. Chem. Phys. 143 (24) (2015) 243128.
- [63] D.K. Lilly, A proposed modification of the Germano subgrid-scale closure method, Phys. Fluids A, Fluid Dyn. 4 (3) (1992) 633-635.
- [64] J. Ling, A. Kurzawski, J. Templeton, Reynolds averaged turbulence modelling using deep neural networks with embedded invariance, J. Fluid Mech. 807 (2016) 155–166.
- [65] J. Ling, J. Templeton, Evaluation of machine learning algorithms for prediction of regions of high Reynolds averaged Navier Stokes uncertainty, Phys. Fluids 27 (8) (2015) 085103.
- [66] Y. Liu, L. Fang, F. Gao, Modification of Spalart–Allmaras model with consideration of turbulence energy backscatter using velocity helicity, Phys. Lett. A 375 (24) (2011) 2377–2381.
- [67] P.P. Mana, L. Zanna, Toward a stochastic parameterization of ocean mesoscale eddies, Ocean Model. 79 (2014) 1-20.
- [68] P.J. Mason, D.J. Thomson, Stochastic backscatter in large-eddy simulations of boundary layers, J. Fluid Mech. 242 (1992) 51-78.
- [69] R. Maulik, K. Fukami, N. Ramachandra, K. Fukagata, K. Taira, Probabilistic neural networks for fluid flow surrogate modeling and data recovery, Phys. Rev. Fluids 5 (10) (2020) 104401.
- [70] R. Maulik, O. San, A stable and scale-aware dynamic modeling framework for subgrid-scale parameterizations of two-dimensional turbulence, Comput. Fluids 158 (2017) 11–38.
- [71] R. Maulik, O. San, A. Rasheed, P. Vedula, Subgrid modelling for two-dimensional turbulence using neural networks, J. Fluid Mech. 858 (2019) 122–144.
- [72] R. Maulik, H. Sharma, S. Patel, B. Lusch, E. Jennings, A turbulent eddy-viscosity surrogate modeling framework for Reynolds-averaged Navier-Stokes simulations, Comput. Fluids (2020) 104777.
- [73] C. Meneveau, J. Katz, Scale-invariance and turbulence models for large-eddy simulation, Annu. Rev. Fluid Mech. 32 (1) (2000) 1–32.
- [74] C. Meneveau, T.S. Lund, The dynamic Smagorinsky model and scale-dependent coefficients in the viscous range of turbulence, Phys. Fluids 9 (12) (1997) 3932–3934.
- [75] A. Mohan, D. Daniel, M. Chertkov, D. Livescu, Compressed convolutional LSTM: an efficient deep learning framework to model high fidelity 3D turbulence, arXiv preprint, arXiv:1903.00033, 2019.
- [76] A.T. Mohan, D. Tretiak, M. Chertkov, D. Livescu, Spatio-temporal deep learning models of 3D turbulence with physics informed diagnostics, J. Turbul. (2020) 1–41.
- [77] P. Moin, K. Mahesh, Direct numerical simulation: a tool in turbulence research, Annu. Rev. Fluid Mech. 30 (1) (1998) 539-578.
- [78] R.D. Moser, S.W. Haering, G.R. Yalla, Statistical properties of subgrid-scale turbulence models, Annu. Rev. Fluid Mech. 53 (2020).
- [79] B. Nadiga, Stochastic vs. deterministic backscatter of potential enstrophy in geostrophic turbulence, in: T. Palmer, P. Williams (Eds.), Stochastic Physics and Climate Modeling, Cambridge University Press, Cambridge, England, 2009, 2010.
- [80] G. Novati, H.L. de Laroussilhe, P. Koumoutsakos, Automating turbulence modelling by multi-agent reinforcement learning, Nat. Mach. Intell. (2021)
- [81] J. O'Brien, J. Urzay, M. Ihme, P. Moin, A. Saghafian, Subgrid-scale backscatter in reacting and inert supersonic hydrogen-air turbulent mixing layers, J. Fluid Mech. 743 (2014) 554.
- [82] P. Orlandi, Fluid Flow Phenomena: A Numerical Toolkit, vol. 55, Springer Science & Business Media, 2012.
- [83] S.A. Orszag, On the elimination of aliasing in finite-difference schemes by filtering high-wavenumber components, J. Atmos. Sci. 28 (6) (1971) 1074.
- [84] S. Pan, K. Duraisamy, Long-time predictive modeling of nonlinear dynamical systems using neural networks, Complexity 2018 (2018).
- [85] S. Pandey, J. Schumacher, K.R. Sreenivasan, A perspective on machine learning in turbulent flows, J. Turbul. (2020) 1–18.
- [86] E.J. Parish, K. Duraisamy, A paradigm for data-driven predictive modeling using field inversion and machine learning, J. Comput. Phys. 305 (2016) 758–774.
- [87] E.J. Parish, K. Duraisamy, A dynamic subgrid scale model for large eddy simulations based on the Mori–Zwanzig formalism, J. Comput. Phys. 349 (2017) 154–175.
- [88] J. Pathak, B. Hunt, M. Girvan, Z. Lu, E. Ott, Model-free prediction of large spatiotemporally chaotic systems from data: a reservoir computing approach, Phys. Rev. Lett. 120 (2) (2018) 024102.

- [89] J. Pathak, M. Mustafa, K. Kashinath, E. Motheau, T. Kurth, M. Day, Using machine learning to augment coarse-grid computational fluid dynamics simulations, arXiv preprint, arXiv:2010.00072, 2020.
- [90] S. Pawar, S.E. Ahmed, O. San, Interface learning in fluid dynamics: statistical inference of closures within micro–macro-coupling models, Phys. Fluids 32 (9) (2020) 091704.
- [91] S. Pawar, O. San, A. Rasheed, P. Vedula, A priori analysis on deep learning of subgrid-scale parameterizations for Kraichnan turbulence, Theor. Comput. Fluid Dyn. (2020) 1–27.
- [92] C. Peyrard, F. Mamalet, C. Garcia, A comparison between multi-layer perceptrons and convolutional neural networks for text image super-resolution, in: VISAPP (1), 2015, pp. 84–91.
- [93] U. Piomelli, Large-eddy simulation: achievements and challenges, Prog. Aerosp. Sci. 35 (4) (1999) 335-362.
- [94] U. Piomelli, W.H. Cabot, P. Moin, S. Lee, Subgrid-scale backscatter in turbulent and transitional flows, Phys. Fluids A, Fluid Dyn. 3 (7) (1991) 1766–1771.
- [95] U. Piomelli, T.A. Zang, C.G. Speziale, M.Y. Hussaini, On the large-eddy simulation of transitional wall-bounded flows, Phys. Fluids A, Fluid Dyn. 2 (2) (1990) 257–265.
- [96] H. Pitsch, Large-eddy simulation of turbulent combustion, Annu. Rev. Fluid Mech. 38 (2006) 453-482.
- [97] S.B. Pope, Turbulent Flows, IOP Publishing, 2001.
- [98] G.D. Portwood, B.T. Nadiga, J.A. Saenz, D. Livescu, Interpreting neural network models of residual scalar flux, J. Fluid Mech. 907 (2021).
- [99] K.G. Pressel, S. Mishra, T. Schneider, C.M. Kaul, Z. Tan, Numerics and subgrid-scale modeling in large eddy simulations of stratocumulus clouds, J. Adv. Model. Earth Syst. 9 (2) (2017) 1342–1365.
- [100] M. Raissi, P. Perdikaris, G.E. Karniadakis, Physics-informed neural networks: a deep learning framework for solving forward and inverse problems involving nonlinear partial differential equations, J. Comput. Phys. 378 (2019) 686–707.
- [101] S. Rasp, M.S. Pritchard, P. Gentine, Deep learning to represent subgrid processes in climate models, Proc. Natl. Acad. Sci. 115 (39) (2018) 9684-9689.
- [102] P. Sagaut, Large Eddy Simulation for Incompressible Flows: An Introduction, Springer Science & Business Media, 2006.
- [103] P. Sagaut, M. Terracol, S. Deck, Multiscale and Multiresolution Approaches in Turbulence-LES, DES and Hybrid RANS/LES Methods: Applications and Guidelines, World Scientific, 2013.
- [104] H. Salehipour, W. Peltier, Deep learning of mixing by two "atoms" of stratified turbulence, J. Fluid Mech. 861 (2019).
- [105] F. Sarghini, G. De Felice, S. Santini, Neural networks based subgrid scale modeling in large eddy simulations, Comput. Fluids 32 (1) (2003) 97-108.
- [106] H. Sarlak, C. Meneveau, J.N. Sørensen, Role of subgrid-scale modeling in large eddy simulation of wind turbine wake interactions, Renew. Energy 77 (2015) 386–399.
- [107] T. Schneider, S. Lan, A. Stuart, J. Teixeira, Earth system modeling 2.0: a blueprint for models that learn from observations and targeted high-resolution simulations, Geophys. Res. Lett. 44 (24) (2017) 12–396.
- [108] V. Shinde, Proper orthogonal decomposition assisted subfilter-scale model of turbulence for large eddy simulation, Phys. Rev. Fluids 5 (1) (2020) 014605.
- [109] G. Shutts, A kinetic energy backscatter algorithm for use in ensemble prediction systems, Q. J. R. Meteorol. Soc. 131 (612) (2005) 3079-3102.
- [110] J. Sirignano, J.F. MacArt, J.B. Freund, DPM: a deep learning PDE augmentation method with application to large-eddy simulation, J. Comput. Phys. 423 (2020) 109811
- [111] J. Smagorinsky, General circulation experiments with the primitive equations: I. The basic experiment, Mon. Weather Rev. 91 (3) (1963) 99-164.
- [112] A.N. Souza, G. Wagner, A. Ramadhan, B. Allen, V. Churavy, J. Schloss, J. Campin, C. Hill, A. Edelman, J. Marshall, et al., Uncertainty quantification of ocean parameterizations: application to the k-profile-parameterization for penetrative convection, J. Adv. Model. Earth Syst. 12 (12) (2020) e2020MS002108.
- [113] R.J. Stevens, L.A. Martínez-Tossas, C. Meneveau, Comparison of wind farm large eddy simulations using actuator disk and actuator line models with wind tunnel experiments, Renew. Energy 116 (2018) 470–478.
- [114] R. Stoffer, C.M. van Leeuwen, D. Podareanu, V. Codreanu, M.A. Veerman, M. Janssens, O.K. Hartogensis, C.C. van Heerwaarden, Development of a large-eddy simulation subgrid model based on artificial neural networks: a case study of turbulent channel flow, Geosci. Model Dev. Discuss. (2020) 1–29.
- [115] A. Subel, A. Chattopadhyay, Y. Guan, P. Hassanzadeh, Data-driven subgrid-scale modeling of forced Burgers turbulence using deep learning with generalization to higher Reynolds numbers via transfer learning, Phys. Fluids 33 (3) (2021) 031702.
- [116] P. Tabeling, Two-dimensional turbulence: a physicist approach, Phys. Rep. 362 (1) (2002) 1-62.
- [117] S. Taghizadeh, F.D. Witherden, S.S. Girimaji, Turbulence closure modeling with data-driven techniques: physical compatibility and consistency considerations, arXiv preprint, arXiv:2004.03031, 2020.
- [118] Z. Tan, T. Schneider, J. Teixeira, K.G. Pressel, Large-eddy simulation of subtropical cloud-topped boundary layers: 2. Cloud response to climate change, J. Adv. Model. Earth Syst. 9 (1) (2017) 19–38.
- [119] J. Thuburn, J. Kent, N. Wood, Cascades, backscatter and conservation in numerical models of two-dimensional turbulence, Q. J. R. Meteorol. Soc. 140 (679) (2014) 626–638.
- [120] G.K. Vallis, Atmospheric and Oceanic Fluid Dynamics, Cambridge University Press, 2017.
- [121] W.T. Verkley, C.A. Severijns, B.A. Zwaal, A maximum entropy approach to the interaction between small and large scales in two-dimensional turbulence, Q. J. R. Meteorol. Soc. 145 (722) (2019) 2221–2236.
- [122] B. Vreman, B. Geurts, H. Kuerten, Large-eddy simulation of the turbulent mixing layer, J. Fluid Mech. 339 (1997) 357-390.
- [123] Z.Y. Wan, P. Vlachas, P. Koumoutsakos, T. Sapsis, Data-assisted reduced-order modeling of extreme events in complex dynamical systems, PLoS ONE 13 (5) (2018) e0197704.
- [124] J.-X. Wang, J.-L. Wu, H. Xiao, Physics-informed machine learning approach for reconstructing Reynolds stress modeling discrepancies based on DNS data, Phys. Rev. Fluids 2 (3) (2017) 034603.
- [125] Z. Wang, K. Luo, D. Li, J. Tan, J. Fan, Investigations of data-driven closure for subgrid-scale stress in large-eddy simulation, Phys. Fluids 30 (12) (2018) 125101.
- [126] R.R. Wilcox, Fundamentals of Modern Statistical Methods: Substantially Improving Power and Accuracy, Springer, 2010.
- [127] J. Wouters, V. Lucarini, Multi-level dynamical systems: connecting the Ruelle response theory and the Mori-Zwanzig approach, J. Stat. Phys. 151 (5) (2013) 850–860.
- [128] J.-L. Wu, K. Kashinath, A. Albert, D. Chirila, H. Xiao, et al., Enforcing statistical constraints in generative adversarial networks for modeling chaotic dynamical systems, J. Comput. Phys. 406 (2020) 109209.
- [129] J.-L. Wu, H. Xiao, E. Paterson, Physics-informed machine learning approach for augmenting turbulence models: a comprehensive framework, Phys. Rev. Fluids 3 (7) (2018) 074602.
- [130] C. Xie, J. Wang, H. Li, M. Wan, S. Chen, Artificial neural network mixed model for large eddy simulation of compressible isotropic turbulence, Phys. Fluids 31 (8) (2019) 085112.
- [131] C. Xie, J. Wang, K. Li, C. Ma, Artificial neural network approach to large-eddy simulation of compressible isotropic turbulence, Phys. Rev. E 99 (5) (2019) 053113.
- [132] C. Xie, J. Wang, E. Weinan, Modeling subgrid-scale forces by spatial artificial neural networks in large eddy simulation of turbulence, Phys. Rev. Fluids 5 (5) (2020) 054606.

- [133] C. Xie, X. Xiong, J. Wang, Artificial neural network approach for turbulence models: a local framework, arXiv preprint, arXiv:2101.10528, 2021.
- [134] Y. Xie, E. Franz, M. Chu, N. Thuerey, tempoGAN: a temporally coherent, volumetric GAN for super-resolution fluid flow, ACM Trans. Graph. 37 (4) (2018) 1–15.
- [135] P. Yeung, S. Pope, An algorithm for tracking fluid particles in numerical simulations of homogeneous turbulence, J. Comput. Phys. 79 (2) (1988) 373-416.
- [136] J. Yosinski, J. Clune, Y. Bengio, H. Lipson, How transferable are features in deep neural networks?, in: Advances in Neural Information Processing Systems, 2014, pp. 3320–3328.
- [137] Y. Zang, R.L. Street, J.R. Koseff, A dynamic mixed subgrid-scale model and its application to turbulent recirculating flows, Phys. Fluids A, Fluid Dyn. 5 (12) (1993) 3186–3196.
- [138] L. Zanna, T. Bolton, Data-driven equation discovery of ocean mesoscale closures, Geophys. Res. Lett. 47 (17) (2020) e2020GL088376.
- [139] Y. Zhou, Eddy damping, backscatter, and subgrid stresses in subgrid modeling of turbulence, Phys. Rev. A 43 (12) (1991) 7049.
- [140] Z. Zhou, G. He, S. Wang, G. Jin, Subgrid-scale model for large-eddy simulation of isotropic turbulent flows using an artificial neural network, Comput. Fluids 195 (2019) 104319.